polymers

MDPI

Article

Electrochemically Deposited Ag/PANI on ITO: Non-Monotonic Disorder–Dispersion Coupling and Enhanced Third-Order Optical Nonlinearity

Mahmoud AlGharram [1,*], Tariq AlZoubi [2,*], Yahia Makableh [2] and Omar Mouhtady [2]

[1] Department of Physics, School of Computing (SC), German Jordanian University, Amman 11180, Jordan
[2] College of Engineering and Technology, American University of the Middle East, Egaila 54200, Kuwait; yahia.makableh@aum.edu.kw (Y.M.); omar.mouhtady@aum.edu.kw (O.M.)
* Correspondence: mahmoud.algharram@gju.edu.jo (M.A.); tariq.alzoubi@aum.edu.kw (T.A.)

Abstract

Conducting polymer–metal nanocomposites are widely investigated as tunable photonic and optoelectronic media; however, reported property trends often remain empirical because electronic disorder at the absorption edge, refractive-index dispersion, free carrier dielectric response, and third-order nonlinearity are rarely quantified within a single, composition-controlled film series. This limitation is particularly relevant for electrochemically grown PANI coatings on transparent conductive substrates, where nanoparticle incorporation can simultaneously enhance polarization while introducing aggregation-driven heterogeneity. Here, Ag/PANI nanocomposite thin films were fabricated directly on indium tin oxide (ITO) by potentiostatic electrodeposition from an aniline/camphorsulfonic acid electrolyte containing controlled Ag nanoparticle loadings (5–15 wt.%). This study addresses the research gap by integrating complementary optical-disorder and dispersion formalisms with dielectric and nonlinear analyses to establish a composition structure optics map for device-relevant films. Ag incorporation narrows the indirect optical gap from 1.98 eV (PANI) to 1.81 eV (5 wt.%), 1.38 eV (10 wt.%), and 1.19 eV (15 wt.%), while markedly broadening the Urbach tail (0.377 eV $\rightarrow$ 1.28–1.64 eV at 5–10 wt.%). Wemple–DiDomenico modeling and Drude-type dielectric dispersion reveal strongly non-monotonic evolution of oscillator energetics and the carrier response, culminating in large bound-electron dielectric constants (ε_∞ up to 469.8) and plasma frequencies (ω_p up to 248 $\times$ 10^{12} Hz) at 15 wt.% Ag. Third-order nonlinearity is substantially enhanced but composition-sensitive: χ^3 increases from 6.73 $\times$ 10^{-9} esu (PANI) to ~7.6 $\times$ 10^{-8} esu at 5 and 15 wt.%, whereas the Kerr coefficient peaks at 25.91 $\times$ 10^{-7} esu for 5 wt.% and is suppressed at intermediate/high loading. These results demonstrate that the optimal nonlinear performance is governed by a disorder–dispersion balance and microstructure-dependent local-field effects rather than the Ag fraction alone.

Keywords: Ag nanoparticles; indirect optical bandgap tuning; PANI; third-order optical nonlinearity; dielectric dispersion and free-carrier response

Check for updates

Academic Editor: Sergi Gallego Rico

Received: 8 March 2026
Revised: 22 March 2026
Accepted: 26 March 2026
Published: 31 March 2026

Copyright: © 2026 by the authors. Licensee MDPI, Basel, Switzerland. This article is an open access article distributed under the terms and conditions of the Creative Commons Attribution (CC BY) license.

1. Introduction

Conducting polymer–metal nanocomposites have emerged as adaptable thin-film platforms in which electronic transport, dielectric polarization, and light–matter interaction can be jointly engineered through interfacial design [1]. By embedding metallic nanoparticles within a π-conjugated host, these hybrids combine the chemical tunability and

low-temperature processability of polymers with the strong electronic polarizability and free-carrier response of metals. Such coupling is particularly attractive for optoelectronic components that demand simultaneous control over optical attenuation, refractive-index dispersion, and nonlinear susceptibility, including photodetectors, electro-optic modulators, optical limiters, and dielectric/optical sensors [2,3].

Among intrinsically conducting polymers, polyaniline (PANI) remains a canonical candidate because its electronic structure can be modulated by protonation and the redox state, enabling large changes in conductivity and optical response without altering the polymer backbone. Nevertheless, pristine PANI films typically exhibit limited optical density and a modest nonlinear performance in the near-infrared, while their dielectric response is strongly influenced by the microstructure and disorder. Incorporation of metallic nanophases offers a route to overcome these limitations. In particular, silver nanoparticles (Ag NPs) can introduce pronounced electronic polarization and broadband extinction through a combination of localized surface plasmon effects, interfacial charge transfer, and enhanced carrier density [4–7]. When appropriately dispersed, Ag NPs may also intensify local electromagnetic fields within the polymer matrix, thereby amplifying third-order nonlinearities relevant to Kerr-type refractive switching and optical limiting. At the same time, increasing metal loading can induce competing effects' aggregation, percolation transitions, and defect-state formation that reshape the band-edge density of states and the dielectric loss landscape. Consequently, the functional outcome is not guaranteed to scale monotonically with filler fraction, and predictive design requires composition-resolved structure property correlations [8,9].

A substantial body of prior work has examined Ag-PANI composites for applications such as sensing, electromagnetic shielding, and conductivity enhancement. However, the optoelectronic literature is comparatively fragmented in two important respects. First, many studies report optical bandgap shifts or refractive-index changes without a unified analysis that connects band-edge tailing (disorder/defect states), dispersion energetics, and free-carrier dielectric behavior within a single materials series [10–12]. Second, third-order nonlinear optical parameters (e.g., χ^3 and the nonlinear refractive index n_2) are often reported either indirectly or in isolation, with limited discussion of how they coevolve with dispersion descriptors (such as Wemple–DiDomenico oscillator parameters) and dielectric loss mechanisms. This leaves a clear gap: a need for a systematic, composition-dependent investigation that links Ag incorporation to (***i***) bandgap narrowing and Urbach tail evolution, (***ii***) refractive-index dispersion and derived dielectric functions, (***iii***) free-carrier contributions in the long-wavelength regime, and (***iv***) the resulting third-order nonlinear optical response ideally for device-relevant thin films grown directly on transparent conductive substrates [13–21].

Previous nonlinear-optical studies on Ag/PANI systems have generally shown that the incorporation of Ag nanostructures enhances the third-order response of PANI by increasing local electromagnetic fields, interfacial polarization, and charge-transfer-assisted delocalization. However, most of these reports were limited to solution-processed composites or cast films and mainly emphasized isolated parameters such as optical limiting, nonlinear absorption, or χ^3, without systematically relating them to band-edge disorder, refractive-index dispersion, and dielectric behavior. A similar trend is evident in broader PANI–metal nanocomposite benchmarks, where fillers such as Au, Ag, Cu, and other metallic nanophases improve polarizability and optical nonlinearity, but the magnitude of enhancement depends strongly on the nanoparticle loading, dispersion quality, interfacial coupling, and aggregation state. These benchmark studies collectively indicate that nonlinear enhancement in PANI–metal systems is not governed by the metal content alone; rather, it emerges from a balance between plasmonic/local-field amplification and

microstructure-induced disorder. This underscores the need for composition-resolved studies that compare the nonlinear performance with dispersion and disorder descriptors within the same Ag/PANI thin-film series.

Electrochemical deposition provides a compelling pathway to address this gap. Compared with solution casting or ex situ blending, potentiostatic electropolymerization can yield conformal PANI coatings with strong adhesion and controllable thickness on conducting substrates, while simultaneously enabling in situ incorporation of nanoparticles from the electrolyte. Direct growth on indium tin oxide (ITO) is particularly advantageous for optoelectronic integration because it couples optical transparency with electrical addressability. Yet, despite these advantages, electrochemically deposited Ag/PANI thin films have not been comprehensively mapped in terms of composition–dispersion–nonlinearity relationships across a controlled Ag loading window. Establishing such relationships is essential for determining whether a given Ag fraction optimizes Kerr nonlinearity, whether band-edge disorder dominates absorption tailing, and how free-carrier polarization reshapes the dielectric spectrum. More broadly, nonlinear-optical enhancement is not limited to compositionally tuned nanocomposites; recent studies have shown that the metasurface and nonlocal meta-optical platforms can greatly amplify nonlinear responses through resonant field confinement, high-Q mode engineering, and tailored wavefront control. In this context, the present Ag/PANI films represent a materials-based route to nonlinear enhancement, where the governing factors are interfacial polarization, charge-transfer-assisted polarizability, and morphology-dependent local-field effects rather than lithographically defined metasurface resonances [22,23].

In this work, Ag/PANI nanocomposite thin films are fabricated by potentiostatic electrodeposition from an aniline/camphorsulfonic acid electrolyte containing controlled Ag NP loadings (5–15 wt.% relative to monomer), yielding uniform films deposited directly on ITO. The central novelty of this study is not merely the preparation of Ag/PANI films, but the integrated, composition-resolved evaluation of their electronic structure and optical response using complementary dispersion and disorder frameworks. Specifically, bandgap evolution is quantified through Tauc analysis alongside Urbach-tail extraction to capture how Ag incorporation modifies the band-edge density of states and electron–phonon coupling signatures. Refractive-index dispersion is interpreted via the Wemple–DiDomenico single-oscillator formalism to extract oscillator energetics and dispersion strength, enabling the comparison of linear polarizability trends across compositions. The dielectric function is then derived from optical constants to assess how polarization storage and loss channels evolve with the wavelength, while the infrared dielectric dispersion is further interpreted using a Drude-type (Spitzer-Fan) approach to elucidate free-carrier contributions. Finally, third-order nonlinear susceptibility and Kerr coefficients are evaluated within a consistent analytical scheme, enabling direct correlation between dispersion parameters, dielectric behavior, and nonlinear optical performance. This combined methodology exposes non-monotonic composition dependencies as an important outcome for rational design by showing that increasing the Ag fraction does not necessarily yield proportional increases in dispersion strength or nonlinear refraction [22–28].

The objectives of this study are therefore to (1) synthesize electrochemically deposited Ag/PANI nanocomposite thin films on ITO with controlled Ag NP loading; (2) establish composition-dependent trends in optical absorption, bandgap narrowing, and Urbach tailing as signatures of defect/disorder evolution; (3) quantify refractive-index dispersion and extract physically meaningful dispersion parameters to describe linear polarizability changes; (4) determine wavelength-dependent dielectric functions and identify the role of free carriers in long-wavelength dielectric dispersion; and (5) evaluate third-order nonlinear optical parameters and relate their enhancement (or suppression) to the underlying

dispersion and microstructural effects. Collectively, these aims provide a structure–optics–nonlinearity map for electrochemically grown Ag/PANI films, supporting their targeted deployment in tunable photonic and optoelectronic devices.

2. Experimental Methods

2.1. Chemicals

Aniline ($C_6H_5NH_2$, Sigma-Aldrich Co. Ltd., St. Louis, MO, USA) was used as received without additional purification. Camphorsulfonic acid (CSA, analytical grade) served as the protonic dopant for the polymerization process. Indium tin oxide (ITO)-coated glass substrates (2.5 cm × 5.5 cm) were supplied by Ossila Ltd. (Sheffield, UK), Silver NPs (Ag NPs) with an average particle size of approximately 20 nm were obtained from US Research Nanomaterials Inc. (Houston, TX, USA). Prior to film growth, the ITO substrates were cleaned by sequential ultrasonication in deionized water, absolute ethanol, and acetone for 5 min in each solvent to remove residual contaminants, improve surface wettability, and promote uniform adhesion of the deposited thin films.

2.2. Thin-Film Depositions

PANI and Ag/PANI nanocomposite thin films were fabricated by potentiostatic electrochemical deposition from an aniline/(CSA) electrolyte. The precursor solution contained 0.25 M aniline and 0.40 M CSA, corresponding to a CSA:aniline molar ratio of 1.6:1. This composition was selected to promote efficient protonation of the growing PANI chains, with CSA functioning both as the acidifying agent and as the dopant counter-ion. Throughout deposition, the electrolyte acidity was maintained at pH ≈ 1.2 to support electrochemically driven oxidative polymerization. After preparation, the aniline/CSA solution was portioned into equal aliquots, and each aliquot was supplemented with a predetermined mass of Ag nanoparticles (Ag NPs). The dispersions were homogenized by vortex mixing for 10 min to minimize particle agglomeration and improve uniformity. Three Ag loadings of 5, 10, and 15 wt.% relative to the aniline monomer were investigated. Electropolymerization was performed in a single-compartment cell at ~25 °C. A stainless-steel counter electrode and an ITO-coated glass working electrode were aligned parallel to each other and separated by a Teflon spacer, defining a 1 cm interelectrode gap. Film growth was initiated by applying a constant potential of 1.3 V for 3 min, yielding PANI and Ag/PANI coatings directly on the ITO substrates. While CSA served as the dopant during deposition, the resulting doping level in the films was not quantified. Film thickness, determined by optical profilometry, was approximately 1500 nm on average. For each composition, optical and electrical measurements were performed on three independently prepared samples, and the reported values represent the mean of these replicates.

2.3. Evaluation of Optical and Structural Properties

The optical response of the deposited films was characterized using a Shimadzu UV–Vis spectrophotometer (UV-100). Normal-incidence transmittance, $T(\lambda)$, was collected over 200–3300 nm and converted to the absorption coefficient (α) using

$$\alpha = -\ln(T)/t \quad (1)$$

where t is the film thickness (nm). The extinction coefficient (k) was subsequently calculated from α according to

$$k = \frac{\alpha\lambda}{4\pi} \quad (2)$$

with λ denoting the incident wavelength (nm). The real refractive index (n), which governs the phase velocity of light within the absorbing film, was determined from the measured reflectance (R) together with k via

$$n = \left(\frac{1+R}{1-R}\right) - \sqrt{\frac{4R}{(1-R)^2} - k^2} \quad (3)$$

Equation (3) corresponds to the physically admissible branch for absorbing thin films. The crystalline structure was examined by X-ray diffraction (XRD) using a Shimadzu 7000 diffractometer (Kyoto, Japan) with Cu K_α radiation (λ = 1.5406 Å) operated at 40 kV and 40 mA. The average crystallite size and microstrain were estimated using the Williamson–Hall method, which deconvolutes peak broadening into size- and strain-related contributions to provide representative crystallite dimensions and internal lattice strain in the nanocomposite films. Fourier-transform infrared (FTIR) spectra were acquired on a PerkinElmer instrument in the 4000–400 cm^{-1} range to assign characteristic vibrational bands and to assess chemical interactions between the PANI matrix and the embedded nanoparticles. The refractive-index dispersion and nonlinear optical response were analyzed within the Wemple–DiDomenico single-effective-oscillator framework, which offers a compact description of $n(\lambda)$ and enables the extraction of key dispersion parameters relevant to nonlinear-optical performance in optoelectronic applications. Surface morphology was evaluated by atomic force microscopy (AFM) in the tapping mode over a 20 μm × 20 μm scan area (512 × 512 pixels). Height maps were first-order plane-leveled and flattened line-by-line prior to quantitative processing. Areal roughness descriptors were including S_a (arithmetic mean height), S_q (root-mean-square height), and S_z (peak-to-valley height; $R_z = z_{max} - z_{min}$). Values reported in Table A1 were extracted from the same scan regions displayed in the AFM images; S_a, S_q, and S_z are given in nm, with S_z additionally reported in μm.

3. Results and Discussion

3.1. Nanocomposites and Film Deposition

Prior to fabricating the nanocomposite coatings, the suitability of ITO substrates for PANI electropolymerization was first evaluated. Electrochemical experiments were performed in a conventional three-electrode cell, employing ITO-coated glass as the working electrode and an aniline/camphorsulfonic acid (CSA) solution as the precursor medium. The ITO electrode was placed in an acidic electrolyte containing the monomer–dopant mixture, enabling in situ oxidative polymerization of aniline directly onto the ITO surface. These preliminary measurements verified the electrochemical responsiveness of the aniline/CSA system on ITO and confirmed that the substrate provides an appropriate platform for subsequent growth of PANI-based nanocomposite thin films [26].

3.2. XRF Characterization

X-ray fluorescence spectroscopy was employed to verify the elemental incorporation of Ag into the PANI matrix and to assess the compositional consistency of the Ag/PANI nanocomposite films. Figure 1 presents the XRF spectra in the photon-energy window of 20–27 keV for films prepared with 5, 10, and 15 wt.% Ag. All spectra are dominated by the characteristic Ag K-series emissions, demonstrating that Ag is present in each nanocomposite composition. Three Ag-related features are clearly resolved. The strongest peak occurs at $h\nu \approx 22.16$ keV, assigned to the Ag-$K_{\alpha1}$ line. Two higher-energy peaks follow at $h\nu \approx 24.94$ keV (Ag-$K_{\beta1}$) and $h\nu \approx 25.45$ keV (Ag-$K_{\beta2}$). The separation between $K_{\alpha1}$ and $K_{\beta1}$ is ≈ 2.78 keV, which matches the expected K-shell transition spacing for Ag and

supports the correctness of the peak assignments. The relative line intensities increase with Ag loading, consistent with a higher Ag areal density in the film. Quantitatively, the maximum $K_{\alpha 1}$ peak intensity rises from ≈1.10 a.u. for the 5 wt.% film (Figure 1a) to ≈1.35 a.u. for 10 wt.% (Figure 1b) and reaches ≈1.80 a.u. for 15 wt.% (Figure 1c). Using these maxima, the $K_{\alpha 1}$ intensity increases by ≈0.25 a.u. from 5→10 wt.% and by ≈0.45 a.u. from 10→15 wt.%, giving an overall $\Delta I \approx 0.70$ a.u. across 5→15 wt.%. A similar, though weaker, loading dependence is observed for the $K\beta_1$ line at ~24.94 keV. The $K\beta_1$ peak increases from ≈0.55 a.u. (5 wt.%) to ≈0.70 a.u. (10 wt.%) and ≈0.70–0.75 a.u. (15 wt.%). Accordingly, the approximate intensity ratio $I(K_{\beta 1})/I(K_{\alpha 1})$ remains in the narrow range ≈0.39–0.50 (0.55/1.10 ≈ 0.50; 0.70/1.35 ≈ 0.52; 0.70/1.80 ≈ 0.39), indicating that the spectral shape is preserved while the overall signal scales with the Ag content [24,28]. The $K_{\beta 2}$ contribution near ~25.45 keV is weaker, reaching ≈0.35 a.u. (5–10 wt.%) and ≈0.45 a.u. (15 wt.%). Beyond the Ag K lines, no additional intense peaks are evident within 20–27 keV, suggesting that no high-Z contaminants contribute significantly in this energy interval. Although XRF in this window does not probe light elements (C, N, H) that form the PANI backbone, the clean Ag K-line signature and its systematic growth with loading provide strong evidence for successful incorporation of Ag nanoparticles and for a composition-dependent increase in Ag content in the deposited films. These XRF results support subsequent structure property correlations, particularly the monotonic enhancement observed in electrical conductivity with an increasing Ag fraction.

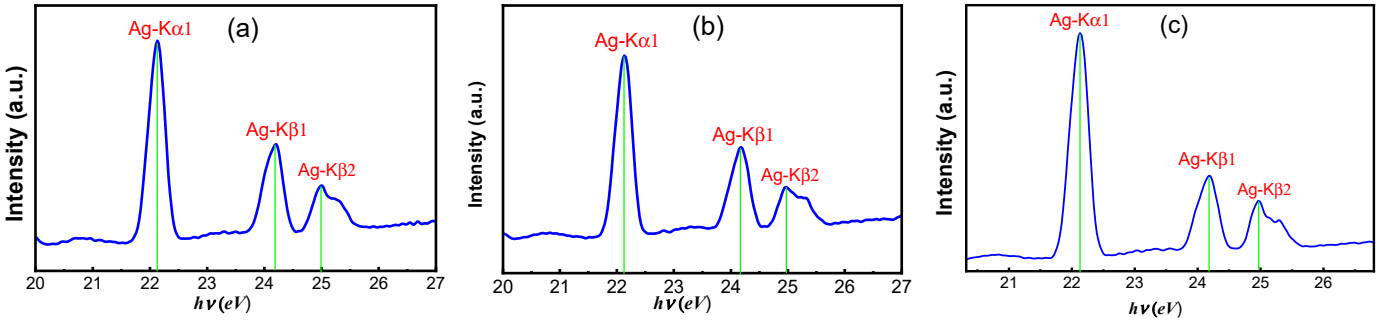


Figure 1. X-ray fluorescence (XRF) spectra of Ag/PANI nanocomposite thin films containing (**a**) 5 wt.%, (**b**) 10 wt.%, and (**c**) 15 wt.% Ag nanoparticles. Distinct Ag K lines are observed at ~22.16 keV (Kα1) and ~24.94 keV (Kβ1), with a Kβ2 feature near ~25.45 keV, confirming successful Ag NP incorporation.

3.3. Atomic Force Microscopy (AFM) Characterization

Figure 2 presents three-dimensional AFM topographies acquired over a 20 × 20 μm^2 region for (a) the pristine PANI and (b) Ag/PANI at 15 wt.%, the nanocomposite film. The pristine PANI exhibits a comparatively smooth, wavy relief with limited sharp features, indicating a more uniform growth front and fewer abrupt height discontinuities. Quantitatively, the pristine surface yields Ra = 0.240088 μm and Rq = 0.303869 μm, with height extrema of +1.13055 μm (maximum) and −1.15284 μm (minimum). The near-zero skewness (−0.000482) suggests an almost symmetric distribution of peaks and valleys around the mean plane, while the slightly negative kurtosis (−0.0756521) implies a modestly flatter than Gaussian height distribution consistent with a surface dominated by broad undulations rather than isolated spikes or pits. In contrast, the nanocomposite film displays a markedly rougher and more heterogeneous landscape, characterized by pronounced ridges and deeper valleys across the same lateral scale. This evolution is reflected in the substantial increase in roughness parameters to Ra = 0.637 μm and Rq = 0.830 μm, together with a large peak-to-valley measure of Rz ≈ 4.74 μm (range 2.389–7.130 μm). Such increases indicate that nanoparticle incorporation (and the associated changes in nucleation

density, local conductivity, and mass transport during growth) intensifies vertical texture development, producing a more corrugated interface. Beyond roughness alone, AFM enables the estimation of the true surface area relative to the projected (planar) area, which is critical when performance depends on the real contact area. For the pristine film, the true surface area is 484.02 μm^2 versus a projected area of 398.439 μm^2, corresponding to an area increase of ≈21.5%. The nanocomposite film shows an even larger enlargement: 517.3 μm^2 true surface area compared with 398.4 μm^2 projected area, i.e., ≈29.8% increase (∼30%). This measurable gain in effective area is expected to (i) increase the density of accessible adsorption/interaction sites, (ii) enhance electrode–electrolyte contact for electrochemical processes, and (iii) promote mechanical interlocking with overlayers or substrates. At the same time, the strong rise in Rq and Rz indicates more severe height excursions, which can introduce local field concentration and nonuniform current pathways; depending on the target application, this may be beneficial (more active sites, improved coupling) or detrimental (greater scattering, localized defects, and percolation inhomogeneity). Overall, the AFM results demonstrate a clear morphological transition from a relatively uniform, wave-like pristine surface to a significantly more textured nanocomposite surface with a higher surface-area enlargement factor. This provides a quantitative microstructural basis for interpreting any concurrent changes in optical response, charge transport, and interfacial sensitivity reported in subsequent sections. Beyond the morphological description, the AFM results provide a microstructural basis for interpreting the optical and nonlinear response of the films. The progressive increase in surface roughness and surface-area development with Ag incorporation is expected to enhance interfacial polarization, increase local electromagnetic field concentration, and introduce greater surface heterogeneity, all of which influence light–matter interaction within the nanocomposite layer. These morphology-driven changes can therefore contribute to the observed variations in refractive-index dispersion, dielectric behavior, and third-order nonlinear optical parameters. Accordingly, the AFM-derived roughness evolution is not merely descriptive, but is physically consistent with the composition-dependent enhancement in the optical and nonlinear performance of the Ag/PANI films. In addition to the three-dimensional AFM topographies, height-distribution histograms were included to provide a statistical representation of the surface–height variation across the scanned area (Figures A1 and A2). These histograms complement the roughness parameters by illustrating the spread, symmetry, and dominant height ranges of the surface features. The broader and more irregular height distribution observed for the Ag-containing films indicates increased surface heterogeneity and more pronounced vertical relief compared with pristine PANI, in agreement with the roughness evolution derived from the AFM analysis. The observed morphological evolution is closely linked to the optical and nonlinear behavior of the Ag/PANI films. With increasing Ag incorporation, the AFM results reveal a progressive increase in surface roughness, granular development, and microstructural heterogeneity, indicating a more complex and highly textured nanocomposite surface. Such changes can enhance interfacial polarization and local field concentration at the Ag/PANI boundaries, while also modifying the effective optical path and light–matter interaction within the film. Consequently, the morphology development provides a structural basis for the observed variations in refractive-index dispersion, dielectric response, optical conductivity, absorption-edge broadening, and third-order nonlinear optical parameters. Therefore, the composition-dependent optical and nonlinear performance of the films can be understood not only in terms of Ag content but also through the accompanying evolution of the nanocomposite microstructure.

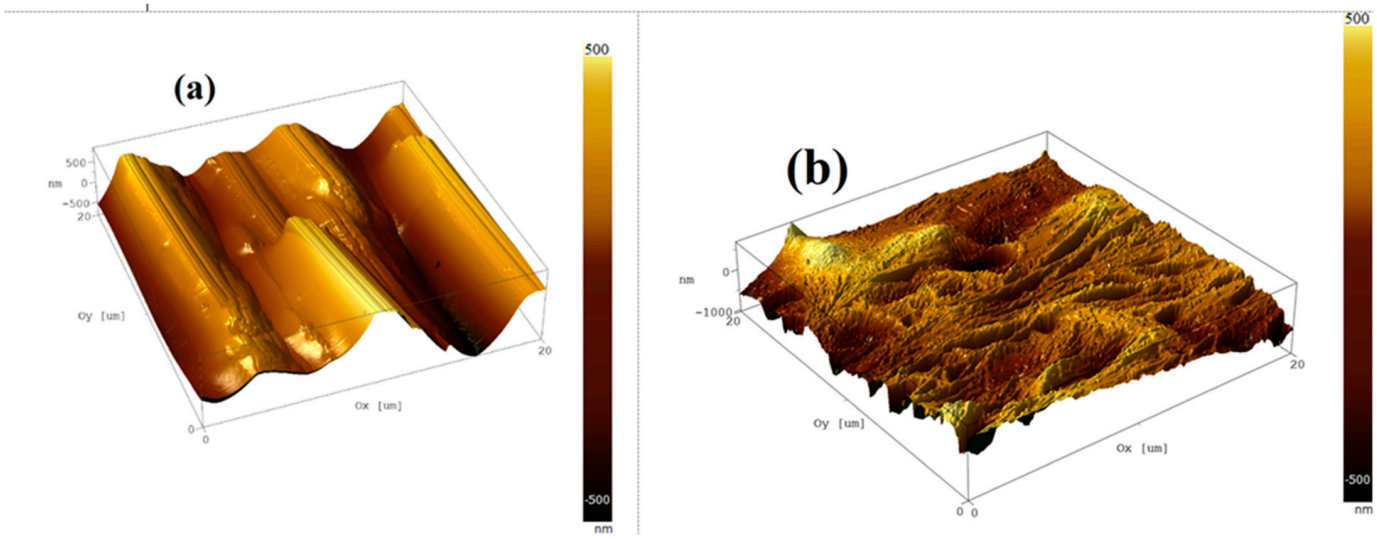


Figure 2. Three-dimensional AFM topography of the films acquired over a 20 × 20 μm^2 area: (**a**) pristine PANI showing a smoother, wavy surface (R_a = 0.240088 μm, R_q = 0.303869 μm; surface area = 484.02 μm^2 vs. projected area = 398.439 μm^2), and (**b**) Ag/PANI at 15 wt.%, with the nanocomposite film showing a rougher morphology (R_a = 0.637 μm, R_q = 0.830 μm, $R_z \approx$ 4.74 μm; surface area = 517.3 μm^2 vs. projected area = 398.4 μm^2, ~30% increase).

3.4. Optical Properties

Figure 3a shows the UV-Vis-NIR absorbance spectra of pristine PANI and Ag/PANI nanocomposite films (5, 10, and 15%) measured over approximately 359–3354 nm. Pristine PANI exhibits comparatively weak absorption with a visible band centered at 450.091 nm (A = 0.293) and a stronger near-IR feature at 867.514 nm (A = 0.333). In the extended near-IR, PANI displays only modest shoulders/maxima at 2305.808 nm (A = 0.210), 2614.338 nm (A = 0.226), and 2777.677 nm (A = 0.221), consistent with a broad polaronic/free-carrier background rather than sharp electronic transitions. Representative absorbance values for PANI are A (500 nm) = 0.278, A (1000 nm) = 0.239, A (2000 nm) = 0.127, A (3000 nm) = 0.203, and A (3300 nm) = 0.096. Incorporation of Ag nanoparticles markedly amplifies the absorbance across the entire spectral window, confirming a substantial increase in optical extinction (absorption and additional loss mechanisms) relative to the pristine polymer. The enhancement is most pronounced in the visible region: at 450.091 nm, the absorbance increases from 0.293 (PANI) to 0.563 (Ag/PANI-5%), 0.650 (Ag/PANI-10%), and 0.748 (Ag/PANI-15%), corresponding to relative gains of +91.9%, +121.6%, and +155.1%, respectively. The Ag/PANI-15% film reaches the highest overall absorbance in the dataset at 450.091 nm (A = 0.748), while Ag/PANI-10% peaks at the same wavelength with A = 0.650, indicating that higher Ag loading intensifies visible-light attenuation. A pronounced loading-dependent evolution is also observed in the near-IR, where the broad carrier-related band strengthens and shifts toward longer wavelengths. Ag/PANI-5% shows its dominant maximum at 894.737 nm (A = 0.567), whereas Ag/PANI-10% and Ag/PANI-15% develop stronger bands at 1130.672 nm (A = 0.621) and 1117.060 nm (A = 0.687), respectively. At 1000 nm, absorbance increases from 0.239 (PANI) to 0.542 (5%), 0.600 (10%), and 0.674 (15%), i.e., enhancements of +127.2%, +151.6%, and +182.4%. This intensification and red-shift of the near-IR response are consistent with an increased density of delocalized charge carriers and stronger polaron/bipolaron contributions promoted by Ag-PANI interfacial interactions. In the long-wavelength region, the spectra reveal a non-monotonic tail behavior. At 2000 nm, the absorbance rises from 0.127 (PANI) to 0.476 (5%), 0.393 (10%), and 0.510 (15%), evidencing a significant growth of the low-energy absorption tail upon Ag incorporation. Beyond approximately 2400–2800 nm, Ag/PANI-10% and Ag/PANI-15%

show more pronounced attenuation, reaching minima of 0.192 at 2723.230 nm (10%) and 0.268 at 2777.677 nm (15%), while Ag/PANI-5% remains comparatively elevated (0.438 at 2768.603 nm). Consequently, at 3300 nm, the absorbance follows the order 5% (0.389) > 15% (0.149) > 10% (0.111) > PANI (0.096), indicating that the 5% loading preserves the strongest far-NIR tail. Collectively, these trends demonstrate that Ag nanoparticles substantially enhance optical extinction in PANI, strengthen and red-shift the carrier-related near-IR band, and modify the sub-gap/low-energy absorption tail in a manner that depends on Ag loading, likely reflecting the combined roles of plasmon-related extinction, interfacial charge transfer, and microstructure/dispersion effects in the nanocomposite films [29].

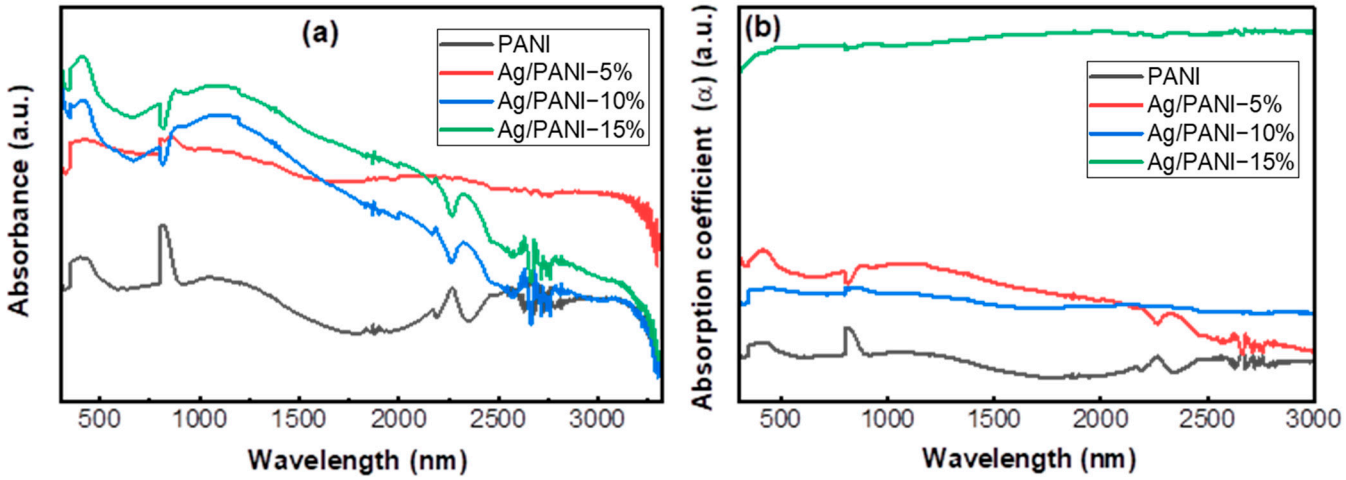


Figure 3. (**a**) Absorbance spectra and (**b**) absorption coefficients for the respective materials.

Figure 3b compares the absorption coefficient spectra, α (a.u.), of pristine PANI and Ag/PANI nanocomposite films (5, 10, and 15%) across approximately 500–3000 nm. The absorption coefficient was obtained from the measured absorbance using the Beer–Lambert relation (Equation (4)).

$$\alpha = 2.303At^{-1} \quad (4)$$

where $A(\lambda)$ is the absorbance at wavelength λ, and t is the film thickness. A clear Ag-loading dependence is evident: incorporation of Ag increases α over the full spectral window and progressively suppresses the wavelength selectivity of the polymer, yielding a more broadband optical response at a higher Ag content. For pristine PANI, α remains low throughout the spectrum and informs a weak near-IR tail. Quantitatively, α equals 0.126 at 500 nm and stays near 0.126 at 1000 nm, then decreases to 0.085 at 1500 nm and reaches 0.068 at 2000 nm. At longer wavelengths, the tail slightly recovers, giving 0.107 at 2500 nm and 0.103 at 3000 nm. The main local maximum occurs at around 834 nm, where α reaches 0.170, while the lowest region is centered near ~1794 nm with α = 0.061. Upon adding 5% Ag, α increases strongly in the visible-near-IR and then gradually declines toward longer wavelengths. At 500 nm, α rises to 0.341 (vs. 0.126 for PANI) and remains high at 1000 nm with α = 0.349. The spectrum then decreases to 0.304 at 1500 nm and 0.257 at 2000 nm, followed by a more pronounced drop in the far-NIR to 0.167 at 2500 nm and 0.130 at 3000 nm. A local maximum is observed near ~418 nm with α = 0.383, and the response exhibits a broad plateau in the ~700–1200 nm interval (average α = 0.339). For 10% Ag, the spectrum becomes more uniform and maintains a moderate α level across the full range. The absorption coefficient is 0.286 at 500 nm, 0.279 at 1000 nm, 0.246 at 1500 nm, 0.242 at 2000 nm, 0.229 at 2500 nm, and 0.225 at 3000 nm, indicating only a gentle decay with the wavelength compared with the 5% film. In the visible region, a local high region occurs near ~411 nm with $\alpha \approx 0.290$, while the near-IR maximum appears at around ~857 nm

with α = 0.291. The small change between 2000 and 3000 nm (0.242 to 0.225) indicates a stable long-wavelength tail for the 10% sample. The non-monotonic behavior of the 10 wt.% film indicates that the measured response is not controlled solely by Ag loading, but also by microstructural factors such as Ag distribution, partial clustering, and interfacial coupling within the PANI matrix. At this intermediate composition, these competing effects can produce a transitional response that deviates from the trend observed for the 5 and 15 wt.% films. The most striking behavior is observed for 15% Ag, which yields an almost wavelength-independent, high absorption coefficient across the entire measured range. The values are α = 0.899 (500 nm), 0.907 (1000 nm), 0.928 (1500 nm), 0.940 (2000 nm), 0.935 (2500 nm), and 0.942 (3000 nm). The average α increases systematically from 0.126 (PANI) to 0.339 (5%), 0.279 (10%), and 0.906 (15%) within 700–1200 nm, and from 0.081 (PANI) to 0.296 (5%), 0.248 (10%), and 0.929 (15%) within 1200–2000 nm, confirming strong broadening and amplification of optical attenuation with an increased Ag fraction. At 2000 nm, the 15% film (α = 0.940) exceeds pristine PANI (α = 0.068) by a factor of approximately 13.8 X. Overall, the spectra demonstrate that Ag addition increases the magnitude of α and reshapes its spectral profile: 5% Ag produces high visible-near-IR absorption followed by a pronounced far-NIR decline, 10% Ag stabilizes the long-wavelength tail at a moderate level, and 15% Ag drives the system into a regime of nearly constant, high α across 500–3000 nm. This evolution is consistent with an increased carrier density and interfacial charge transfer in Ag/PANI, together with broadband optical losses introduced by the metallic phase (including plasmon-related extinction and microstructure-dependent scattering), which become increasingly dominant at higher Ag loading [30].

Figure 4 presents the Tauc analysis of the optical transition for pristine PANI and Ag/PANI nanocomposite films (5, 10, and 15 wt.%) by plotting $(\alpha h\nu)^2$ as a function of photon energy ($h\nu$). The optical bandgap was extracted from the linear portion of each curve near the absorption edge by extrapolating the fitted straight line to the energy axis ($(\alpha h\nu)^2 \rightarrow 0$), following the Tauc relation [30]:

$$(\alpha h\nu)^{1/n} = \beta(h\nu - E_g) \quad (5)$$

where α is the absorption coefficient, $h\nu$ is the photon energy, β is a proportionality constant, and E_g is the optical energy gap. In the representation used in Figure 4, the ordinate is $(\alpha h\nu)^2$, corresponding to $n = 1/2$ in Equation (5). The Tauc plots exhibit a clear, Ag-loading-dependent displacement of the absorption edge toward lower photon energies, demonstrating progressive bandgap narrowing upon the incorporation of Ag nanoparticles. The extracted energy-gap values (Table 1) decrease systematically from E_g = 1.98 eV for pristine PANI to 1.81 eV for Ag/PANI—5 wt.%, 1.38 eV for Ag/PANI—10 wt.%, and 1.19 eV for Ag/PANI—15 wt.%. Relative to pristine PANI, the absolute reductions are 0.17 eV (5 wt.%), 0.60 eV (10 wt.%), and 0.79 eV (15 wt.%), which correspond to decreases of 8.59%, 30.30%, and 39.90%, respectively. The largest incremental change occurs when increasing the Ag content from 5 to 10 wt.% (ΔE_g = 0.43 eV, a 23.76% reduction relative to the 5 wt.% film), whereas the change from 10 to 15 wt.% is smaller (ΔE_g = 0.19 eV, 13.77% relative to the 10 wt.% film). These quantitative trends are consistent with Ag-induced modification of the polymer matrix's electronic structure. In particular, the observed bandgap narrowing, together with the broadening of the Urbach tail and the strengthening of low-energy optical absorption, suggests an increase in localized interfacial/disorder-related states near the band edge and a possible enhancement of carrier delocalization within the Ag/PANI nanocomposite. Therefore, this interpretation is inferred from the combined optical-disorder and conductivity trends rather than claimed as a direct electronic-structure measurement. In Ag/PANI, interfacial interactions between metallic nanoparticles and the π-conjugated backbone can promote charge transfer and increase the density of

polaronic and bipolaronic states, effectively extending the absorption tail to lower energies and shifting the Tauc intercept to smaller E_g. The monotonic narrowing from 1.98 to 1.19 eV therefore supports a transition from a wider gap polymer response to a more metallic/strongly doped electronic structure at higher Ag loading, consistent with the broadband optical strengthening observed in the corresponding absorbance and absorption-coefficient spectra [27–33].

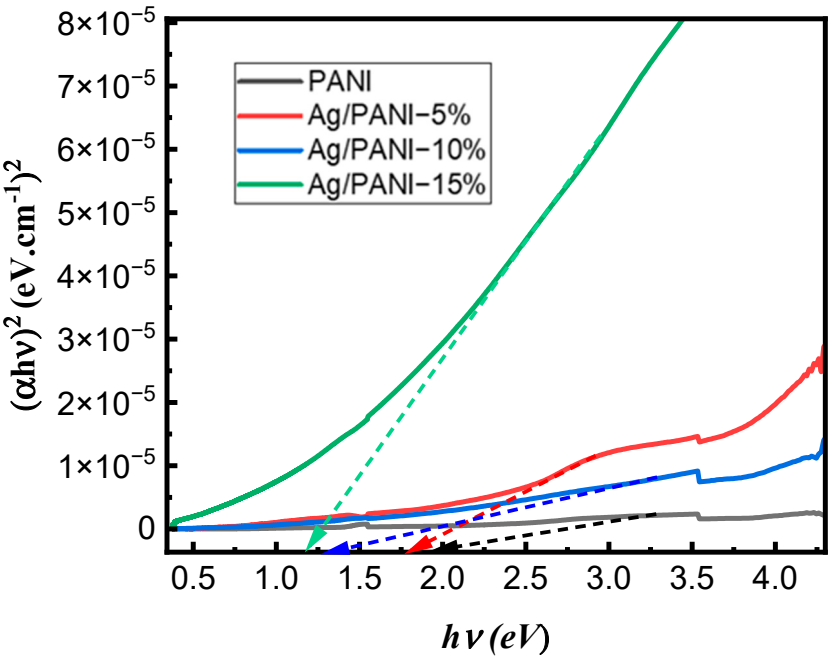


Figure 4. Analysis of $(\alpha h\nu)^2$ as a function of incident photon energy for PANI and nanocomposites.

Table 1. Comparative analysis of electronic structural parameters in PANI and nanocomposites.

Sample	Indirect Energy Gap (E_g) (eV)	Urbach Energy (meV)	Steepness Parameter (γ) (eV^{-1})	Strength of Electron–Phonon (E_{e_p}) (eV)
PANI	1.98	377	0.06	10.7
Ag/PANI—5 wt.%	1.81	1280	0.02	36.2
Ag/PANI—10 wt.%	1.38	1640	0.01	46.4
Ag/PANI—15 wt.%	1.19	Not reliable	***	***

Figures 5 and 6 summarize the Urbach-tail analysis for pristine PANI and Ag/PANI nanocomposite films (5, 10, and 15 wt.% Ag), and Table 1 lists the derived disorder- and coupling-related parameters. In the sub-bandgap (exponential) absorption region, the absorption coefficient follows the Urbach relation:

$$\alpha = \alpha_0 \, exp(h\nu/E_U) \quad (6)$$

where α_0 is a pre-exponential factor, $h\nu$ is the photon energy, and E_U is the Urbach energy. Taking the natural logarithm gives $ln(\alpha) = ln(\alpha_0) + (h\nu/E_U)$, so E_U is obtained from the inverse slope of the linear part of the $ln(\alpha)$ versus $h\nu$ plot (Figure 5).

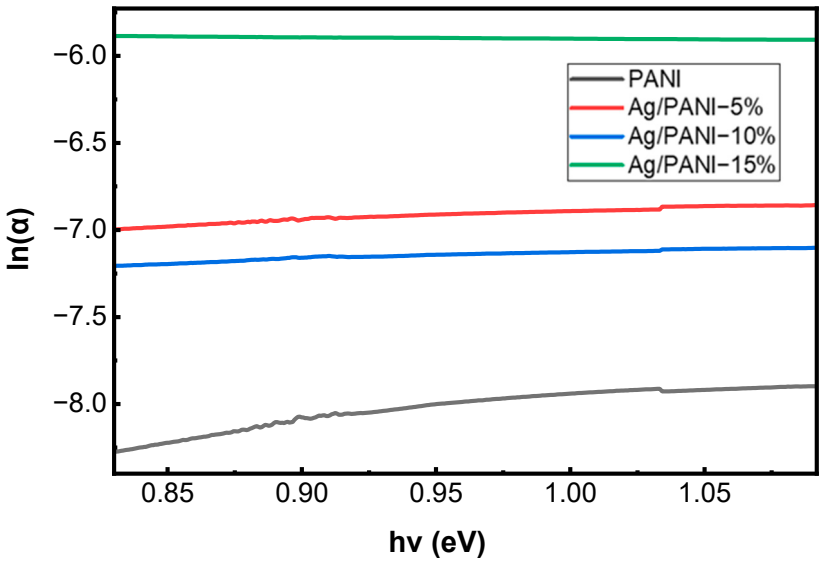


Figure 5. Urbach energy variation with incident photon energy in PANI and nanocomposites.

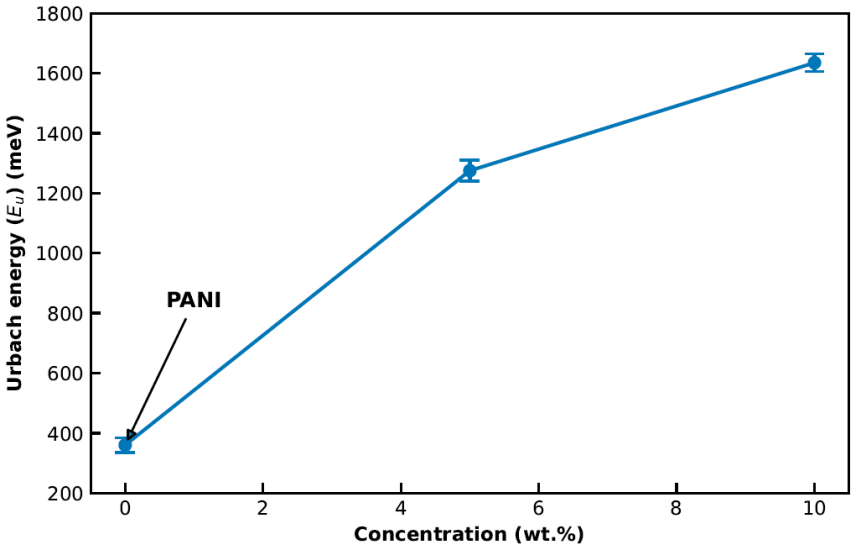


Figure 6. Variation in Urbach energy (E_U) as a function of nanofiller concentration for PANI and its nanocomposites.

Figure 5 shows that pristine PANI exhibits the steepest $ln(\alpha)$ versus $h\nu$ dependence (largest slope), consistent with the smallest Urbach energy and a relatively sharper absorption edge. Quantitatively, Table 1 yields E_U = 377 meV (0.377 eV) for PANI. The corresponding Urbach slope is $1/E_U$ = 2.652 eV^{-1}, indicating a comparatively narrow distribution of localized tail states. Upon incorporating Ag, the $ln(\alpha)$ versus $h\nu$ curves shift upward and become less steep, evidencing a broadening of the exponential tail. Specifically, E_U increases to 1280 meV (1.280 eV) for Ag/PANI—5 wt.% and to 1640 meV (1.640 eV) for Ag/PANI—10 wt.% (Table 1), which reduces the Urbach slopes to 0.781 and 0.610 eV^{-1}, respectively. Relative to pristine PANI, E_U rises by +903 meV at 5 wt.% (an increase of 239.5%) and by +1263 meV at 10 wt.% (an increase of 335.0%). The incremental change from 5 to 10 wt.% is +360 meV (28.1%), confirming that the dominant broadening of the sub-gap tail occurs already at moderate Ag loading. Figure 6 visualizes the same trend by plotting E_U versus nanofiller concentration: E_U increases from 377 meV at 0 wt.% (PANI) to 1280 meV at 5 wt.% and 1640 meV at 10 wt.%, corresponding to ≈3.40× and ≈4.35× amplification relative to the pristine polymer. These increases indicate a substantial rise in

structural/electronic disorder and a higher density of localized states in the gap region, which is consistent with the formation of additional tail states at Ag/PANI interfaces and with enhanced carrier localization arising from nanofiller-induced microstructural heterogeneity. The steepness parameter γ ($\gamma = k_B\ T/E_U$) (eV^{-1}) [31] (Table 1) decreases monotonically with Ag content, from 0.06 eV^{-1} for PANI to 0.02 eV^{-1} for 5 wt.% and 0.01 eV^{-1} for 10 wt.%, i.e., reductions by factors of 3 and 6 relative to pristine PANI. In parallel, the strength of electron–phonon interaction E_{e_p} ($E_{e_p} = 2/3\ \gamma$ [31]) increases from 10.7 eV (PANI) to 36.2 eV (5 wt.%) and 46.4 eV (10 wt.%), representing increases of 3.38× and 4.34×, respectively. The simultaneous increase in E_U and E_{e_p}, together with the decrease in γ, supports stronger coupling between electronic states and lattice/segmental vibrations and a broader energetic spread of localized states as the Ag concentration rises. For Ag/PANI—15 wt.%, Table 1 reports the Urbach parameters as "not reliable" (E_U), with an undefined γ and E_{e_p} (***). This limitation is consistent with the deviation from a well-defined linear Urbach regime in $ln(\alpha)$ versus $h\nu$ at high loading, where strong metallic extinction, aggregation-related scattering, and/or saturation of sub-gap absorption can obscure the exponential tail needed for robust fitting. The lack of a reliable Urbach–energy fit for the 15 wt.% Ag/PANI film does not negate the overall disorder-related trend observed at lower Ag contents. Rather, it indicates that at the highest loading, the absorption-edge region becomes too complex to be adequately described by a single-exponential Urbach model. The progressive increase in E_U from pristine PANI to 5 wt.% and 10 wt.% already confirms substantial broadening of the absorption edge with Ag incorporation. For the 15 wt.% film, the fitting limitation is itself physically meaningful, as it suggests the coexistence of multiple loss contributions, including strong metallic extinction, interfacial absorption, aggregation-related scattering, and increased edge-state complexity. Therefore, this sample is better interpreted as marking the onset of a more optically complex regime, rather than providing a quantitatively reliable E_U value within the simple Urbach framework. Overall, the combined results in Figures 5 and 6 and Table 1 demonstrate that Ag incorporation substantially broadens the Urbach tail (E_U: 0.377 → 1.640 eV), reduces the absorption-edge steepness (γ: 0.06 → 0.01 eV^{-1}), and strengthens electron–phonon interaction (E_{e_p}: 10.7 → 46.4 eV), confirming a pronounced increase in disorder-driven tail states and interfacial coupling in the Ag/PANI nanocomposite system.

- **Optical constants: Extinction coefficient (*K*) and refractive index (*n*)**

Figure 7 presents the optical constants of pristine PANI and Ag/PANI nanocomposite films (5–15 wt.% Ag) as functions of wavelength, including (a) the extinction coefficient (K) and (b) the refractive index (n) over the visible-near-IR window (≈500–3000 nm). In both panels, Ag incorporation produces a marked strengthening of optical loss and dispersion, with the magnitude and wavelength dependence controlled by the Ag loading. Pristine PANI exhibits low K values throughout the spectrum, increasing from K (500 nm) = 0.010 to K (3000 nm) = 0.070, with a gradual rise in the long-wavelength region. Introducing Ag elevates K across the full window. At 500 nm, K increases to 0.036 (5%), 0.029 (10%), and 0.102 (15%), i.e., enhancements of 3.45×, 2.83×, and 9.86× relative to PANI. The Ag/PANI—5% film increases up to K = 0.120 at 2000 nm and then decreases to 0.089 at 3000 nm, indicating that optical loss peaks in the mid-IR/near-IR range for this loading [34,35].

In contrast, Ag/PANI—10% increases more monotonically from 0.029 (500 nm) to 0.159 (3000 nm), reaching a maximum $K \approx 0.164$ near 3100 nm. The Ag/PANI—15% film shows the strongest and most rapidly rising loss, increasing from 0.102 at 500 nm to 0.674 at 3000 nm, with a maximum $K \approx 0.686$ near 3078 nm; at 3000 nm, this corresponds to ≈9.65× the PANI value, evidencing a transition to a highly lossy optical response at high Ag content. Pristine PANI shows weak dispersion with $n \approx 2.52$ at 500 nm, a

shallow minimum $n \approx 2.07$ near 1712 nm, and $n \approx 2.38$ at 3000 nm, consistent with a relatively low-loss polymer matrix. Ag NP addition substantially raises n and amplifies its wavelength dependence. For Ag/PANI—5%, n increases from 4.912 at 500 nm to 6.014 at 800 nm, then drops to 3.603 at 1000 nm before rising to a maximum $n \approx 8.194$ near 2354 nm and ending at n (3000 nm) = 6.706. The Ag/PANI—10% film exhibits a lower n at short wavelengths (n (500 nm) = 2.278) and a pronounced growth toward the near-IR (n (2500 nm) = 4.572 and n (3000 nm) = 4.907), with an overall increase of +2.629 between 500 and 3000 nm. The strongest dispersion is observed for Ag/PANI—15%, where n rises from 3.563 (500 nm) to 9.599 (2500 nm) and 12.726 (3000 nm), with a peak $n \approx 12.829$ around 2663 nm and strong oscillatory features in the 2600–2800 nm region. Such high-n, highly dispersive behavior at 15% is consistent with intense free-carrier/metal-related optical response and microstructure-dependent scattering in the strongly loaded nanocomposite. Overall, Figure 7 demonstrates that an increasing Ag concentration markedly enhances the extinction coefficient and increases the refractive index, shifting the system toward a more optically dense and lossy medium. The progressive rise in K and n especially for 15 wt.% supports stronger electronic polarization and broadband attenuation, plausibly driven by Ag-induced carrier density, interfacial charge transfer with the π-conjugated PANI backbone, and increased disorder/heterogeneity at higher nanoparticle loading [30].

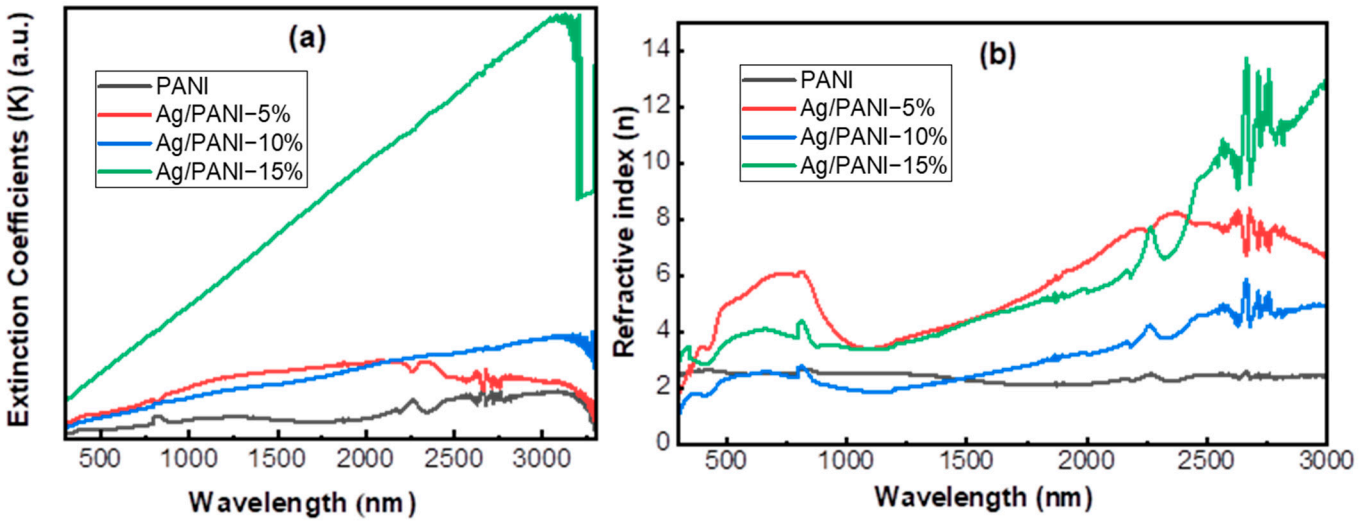


Figure 7. Optical constants of PANI and Ag/PANI (5–15 wt.%): (**a**) extinction coefficient (K) and (**b**) refractive index (n) as functions of wavelength, highlighting enhanced optical loss and stronger dispersion with higher Ag content.

- **Optical Anisotropy and Birefringence Analysis**

Optical anisotropy in the PANI and Ag/PANI films can be quantified using the dispersion of the refractive index, $n(\lambda)$, extracted from Figure 7b. For each specimen, the ordinary index (n_0) was approximated by the minimum $n(\lambda)$ within the measured window (≈500–3000 nm), while the extraordinary index (n_e) was approximated by the maximum $n(\lambda)$ in the same range. The birefringence was then evaluated as $\Delta n = n_e - n_0$, and a uniaxial average refractive index was estimated using $n^- = (2n_0 + n_e)/3$. This approach provides a consistent, figure-based measure of the magnitude of optical anisotropy and its dependence on Ag loading. Pristine PANI exhibits a weakly dispersive refractive index with $n_0 = 2.070$ and $n_e = 2.545$, giving a small birefringence $\Delta n = 0.475$ and an average index $n^- = 2.228$. The low Δn indicates limited structural anisotropy and a relatively homogeneous polymer matrix, where the optical response is dominated by the π-conjugated backbone with modest long-wavelength dispersion. Introducing Ag NPs

amplifies anisotropy substantially. For Ag/PANI—5 wt.%, the refractive index spans from n_0 = 3.603 to n_e = 8.194, yielding Δn = 4.591 and n^- = 5.133. Relative to pristine PANI, Δn increases by 4.116 (a factor of 9.66×), while the average index rises by +2.905 (from 2.228 to 5.133, +130.4%). The large index spread and the pronounced n maximum indicate strong optical polarizability and enhanced dispersion, consistent with significant interfacial polarization and microstructural anisotropy generated by the metallic nanophase within the PANI host. For Ag/PANI—10 wt.%, the refractive index range is n_0 = 1.932 to n_e = 4.907, corresponding to Δn = 2.975 and n^- = 2.924. Compared with PANI, Δn increases by 2.500 (6.26×), and n^- increases by +0.696 (+31.2%). Notably, the presence of the lowest n_0 value (1.932) together with a moderate n_e suggests that, at 10 wt.% loading, the optical response reflects a balance between increased carrier-related dispersion and microstructure-dependent effects (e.g., porosity, percolation, or nanoparticle distribution) that can reduce the effective index at certain wavelengths. The strongest optical anisotropy is observed for Ag/PANI—15 wt.%, where n_0 = 3.419 and n_e = 12.829, giving an exceptionally large birefringence Δn = 9.410 and n^- = 6.556. Relative to PANI, Δn increases by 8.935 (19.81×) and n^- increases by +4.328 (+194.3%).

The very high n_e and large Δn are consistent with a highly dispersive, optically dense response dominated by Ag-related free-carrier/metallic polarization and strong interfacial charge-transfer effects. The pronounced oscillations in $n(\lambda)$ reported for the high-loading film in the 2600–2800 nm region further support the presence of strong wavelength-dependent dispersion driven by microstructure and increased optical loss mechanisms in the nanocomposite. Overall, the birefringence evolves nonlinearly with Ag concentration: Δn increases from 0.475 (PANI) to 4.591 (5 wt.%), decreases to 2.975 (10 wt.%), and then rises sharply to 9.410 (15 wt.%). This non-monotonic progression indicates that anisotropy is governed not only by nanoparticle fraction but also by dispersion state and mesoscale morphology. Moderate Ag NP loading can generate strong interfacial polarization and anisotropic domains (large Δn at 5 wt.%), whereas further loading may alter packing/porosity or percolation pathways (lower Δn at 10 wt.%), before ultimately transitioning to a strongly metal-influenced optical regime at 15 wt.%, where polarization and dispersion dominate (Δn = 9.410). These results confirm that Ag NP incorporation significantly enhances optical anisotropy and birefringence in PANI-based films, which is relevant for photonic components requiring tunable refractive indices and polarization-dependent optical response (Table 2).

Table 2. Estimated birefringence and extraordinary refractive index.

Sample	Average Refractive Index (n^-)	Birefringence (Δn)	Estimated n_e (max n)	Estimated n_0 (min n)
PANI	2.228	0.475	2.545	2.070
Ag/PANI—5 wt.%	5.133	4.591	8.194	3.603
Ag/PANI—10 wt.%	2.924	2.975	4.907	1.932
Ag/PANI—15 wt.%	6.556	9.410	12.829	3.419

- **The optical conductivity**

Figure 8a depicts the spectral variation in the optical conductivity, σ_{opt} (S^{-1}), for pristine PANI and Ag/PANI nanocomposite as a function of photon energy ($h\nu$). The optical conductivity was evaluated from the absorption coefficient (α) and refractive index (n) according to

$$\sigma_{opt} = \frac{\alpha n c}{4\pi} \quad (7)$$

where is the speed of light in a vacuum. Because σ_{opt} scales linearly with both α and n, any Ag-induced enhancement in optical loss (α) and optical density (n) is expected to

translate directly into higher σ_{opt}, especially in the low-energy region where free-carrier and polaronic contributions dominate. The spectra show a pronounced, loading-dependent increase in σ_opt over the entire photon-energy window. At $h\nu$ = 0.50 eV, σ_{opt} increases from 1.32 × 10^4 S^{-1} for PANI to 1.24 × 10^5 S^{-1} for Ag/PANI—5%, 5.70 × 10^4 S^{-1} for Ag/PANI—10%, and 3.71 × 10^5 S^{-1} for Ag/PANI—15%. Relative to PANI at the same energy, these correspond to enhancement factors of 9.42× (5%), 4.33× (10%), and 28.19× (15%). This large amplification at low $h\nu$ is consistent with the strong increase in long-wavelength extinction and refractive index reported for the higher-loading nanocomposites. In the intermediate-energy region, σ_{opt} remains clearly separated by composition and exhibits a broad, slowly varying response. At $h\nu$ = 2.00 eV, σ_{opt} equals 2.12 × 10^4 S^{-1} (PANI), 1.26 × 10^5 S^{-1} (5%), 5.01 × 10^4 S^{-1} (10%), and 2.56 × 10^5 S^{-1} (15%), meaning that the 15 wt.% film sustains a 12.03× higher σ_{opt} than pristine PANI. At $h\nu$ = 3.00 eV, σ_{opt} is 2.93 × 10^4 S^{-1} (PANI), 9.51 × 10^4 S^{-1} (5%), 3.74 × 10^4 S^{-1} (10%), and 1.81 × 10^5 S^{-1} (15%). Thus, the 15 wt.% film maintains a 6.16× enhancement relative to PANI while the 5 wt.% film remains 3.24× higher than PANI. A key spectral feature is the strong low-energy conductivity of the 15 wt.% nanocomposite.

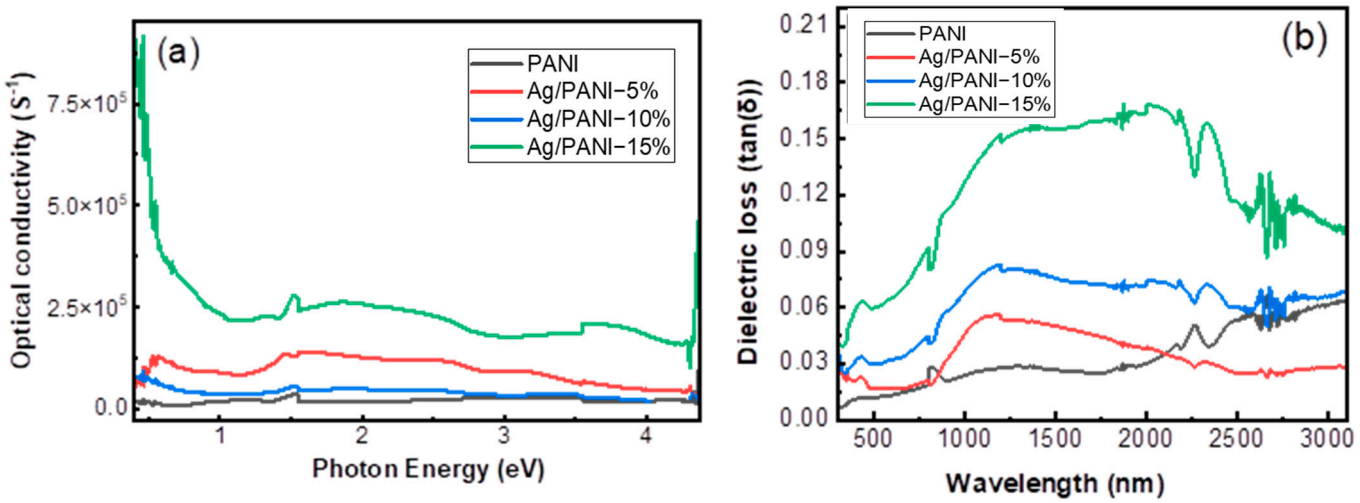


Figure 8. Representation of (**a**) optical conductivity and (**b**) dielectric loss ($tan(\delta)$) for PANI and nanocomposites.

The extracted maximum optical conductivity for Ag/PANI—15% reaches 8.23 × 10^5 S^{-1} at the lowest-energy edge of the plot and then decreases to ~2.21 × 10^5 S^{-1} by 1.00 eV. This behavior is characteristic of a free-carrier-dominated optical response, where σ_{opt} is highest at low photon energies and diminishes as the excitation energy moves away from the carrier-related absorption tail. In contrast, Ag/PANI—5% exhibits its highest σ_{opt} in the mid-energy region, peaking at 1.44 × 10^5 S^{-1} around $h\nu \approx$ 1.48 eV, then gradually declining toward higher energies. At the higher-energy end ($h\nu \approx$ 4.00 eV), σ_{opt} remains elevated for the Ag-rich film: 1.77 × 10^5 S^{-1} (15%) compared with 2.47 × 10^4 S^{-1} (PANI), corresponding to a 7.17× enhancement. Minor fluctuations and edge spikes near the plot boundaries are attributed to reduced signal stability and numerical sensitivity in α and n extraction at the spectral limits, and therefore the central-energy trends provide the most reliable comparison. Overall, Figure 8a demonstrates that Ag NP incorporation drives a substantial, composition-controlled increase in optical conductivity across the measured photon energies. The hierarchy Ag/PANI—15% ≫ Ag/PANI—5% > Ag/PANI—10% > PANI is consistent with the simultaneous Ag-induced enhancement of extinction (α) and refractive index (n). The large low-energy σ_{opt} of the 15 wt.% film supports a transition toward a more metal-influenced, carrier-rich optical response, likely arising from intensified

interfacial charge transfer, higher free-carrier density, and stronger electronic delocalization in the Ag/PANI network [34].

3.5. Dielectric Properties

3.5.1. Wavelength-Dependent Dielectric Response

Figure 9 resolves the wavelength-dependent complex dielectric response of PANI and Ag/PANI nanocomposite into the real part, ε_r, and the imaginary part, ε_i, over the broad near-UV/visible to near-IR window (≈400–3200 nm). The dielectric function is expressed as a complex quantity:

$$\varepsilon = \varepsilon_r + i\varepsilon_i \quad (8)$$

where ε_r describes the ability of the medium to store electromagnetic energy through polarization, while ε_i represents dielectric loss associated with energy dissipation. Importantly, ε_r and ε_i can be derived directly from the optical constants (refractive index n and extinction coefficient k) through

$$\varepsilon_r = n^2 - k^2 \quad (9)$$

$$\varepsilon_i = 2nk \quad (10)$$

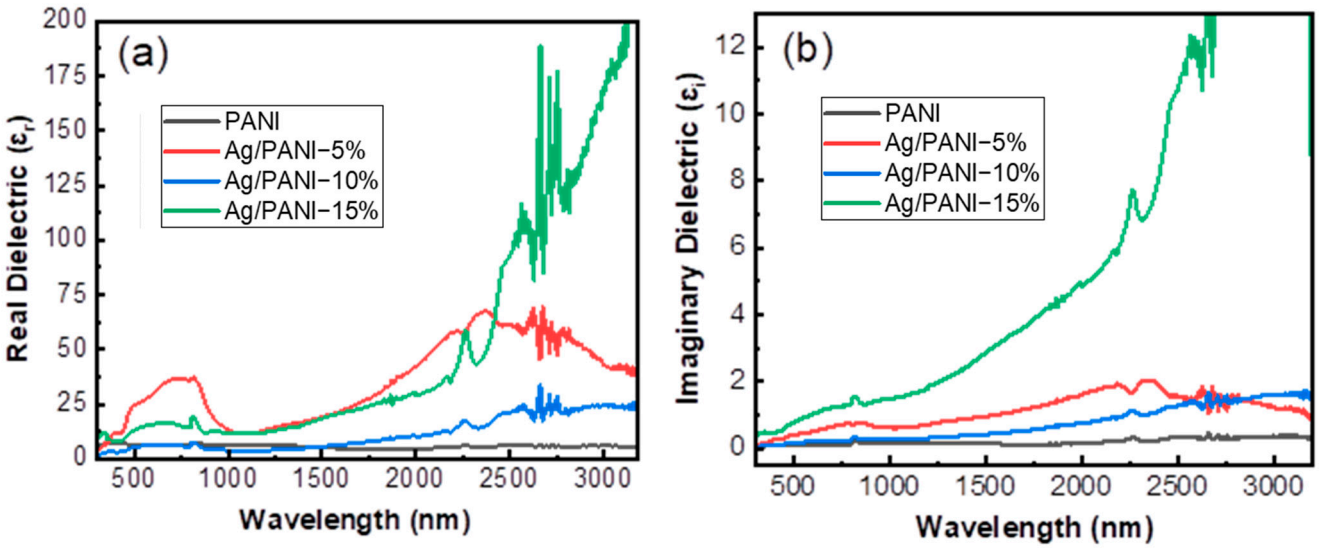


Figure 9. (**a**) Real dielectric (ε_r) and (**b**) imaginary dielectric (ε_i) for PANI and nanocomposites.

Thus, increases in n primarily elevate ε_r, whereas increases in k (optical loss) strongly amplify ε_i. This linkage is especially relevant here because Ag NP loading simultaneously modifies both n and k, thereby reshaping polarization and loss. Pristine PANI exhibits a low-magnitude and weakly dispersive ε_r throughout most of the spectrum, indicating modest polarizability and limited long-wavelength dispersion. Quantitatively, ε_r (PANI) is 4.110 at 500 nm and remains 4.110 at 1000 and 1500 nm, before dropping to 2.740 at 2000 nm and recovering slightly to 3.196 at 2500–3000 nm. The narrow range (2.740–4.110) reflects a relatively stable electronic polarization response, consistent with a polymer matrix where dispersion is governed mainly by π–π* transitions at higher energies and polaronic contributions at lower energies without a strong metallic component. Introducing Ag nanoparticles substantially increases ε_r and makes it strongly wavelength-dependent, evidencing enhanced electronic and interfacial polarization. For Ag/PANI—5 wt.%, ε_r rises from 8.676 (500 nm) to 13.699 (1000 nm) and 14.612 (1500 nm), then accelerates to 35.160 at 2000 nm and reaches a maximum of 58.904 at 2500 nm before decreasing to 48.402 at 3000 nm. Relative to PANI, the enhancement factors at 2000 nm and 2500 nm are

12.83× (35.160/2.740) and 18.43× (58.904/3.196), respectively. This sharp long-wavelength growth indicates that Ag incorporation increases the effective polarizability, likely through a (**i**) higher carrier density, (**ii**) Maxwell–Wagner-type interfacial polarization at Ag/PANI boundaries, and (**iii**) stronger dispersion as the system approaches a more conductive regime. The Ag/PANI—10 wt.% sample shows a distinct profile: ε_r is comparatively low at short wavelengths (0.457 at 500 nm, 1.370 at 1000 nm) but increases steadily toward the near-IR (2.283 at 1500 nm, 7.306 at 2000 nm, 15.525 at 2500 nm, and 21.461 at 3000 nm). The growth from 500 to 3000 nm equals +21.004, indicating pronounced long-wavelength dispersion even though the absolute ε_r values are smaller than those of 5% at 2000–2500 nm. This behavior implies that the effective n^2 term (Equation (9)) increases progressively with the wavelength and that microstructural factors (e.g., porosity, percolation topology, or nanoparticle distribution) can reduce the effective ε_r in the visible while still enabling strong near-IR polarization. The strongest ε_r enhancement is observed for Ag/PANI—15 wt.%, which transitions to a highly dispersive dielectric response at long wavelengths. ε_r increases from 5.479 (500 nm) to 9.589 (1000 nm) and 13.242 (1500 nm), then rises to 25.114 at 2000 nm, 61.187 at 2500 nm, and reaches 146.119 at 3000 nm. At 3000 nm, ε_r (15%) exceeds ε_r (PANI) by 45.71 × (146.119/3.196), evidencing a dramatic increase in optical polarizability and a strong low-energy response consistent with metal-assisted dispersion and carrier-rich behavior. The sharp increase and oscillatory features near the far-right spectral edge suggest that extraction becomes sensitive to measurement noise and to the strong loss regime; nevertheless, the magnitude and trend clearly demonstrate that a high Ag content drives ε_r to very large values in the near-IR.

Pristine PANI exhibits very low ε_i values, consistent with weak optical loss. ε_i (PANI) equals 0.237 at 500 nm, remains 0.297 at 1000–2000 nm, and then increases slightly to 0.416 at 2500 nm and 0.505 at 3000 nm. The modest long-wavelength rise indicates increasing absorption/loss at low photon energies, but the absolute values remain small, confirming that pristine PANI is comparatively low-loss in this window. Ag NP incorporation increases ε_i markedly and, in most cases, shifts loss toward longer wavelengths. For Ag/PANI—5 wt.%, ε_i rises from 0.386 at 500 nm to 0.772 at 1000 nm, 1.039 at 1500 nm, and 1.632 at 2000 nm, reaching 1.692 at 2500 nm before slightly decreasing to 1.543 at 3000 nm. Relative to PANI, ε_i is enhanced by 5.49× at 2000 nm (1.632/0.297) and by 4.07× at 2500 nm (1.692/0.416). This evolution indicates that k increases strongly with Ag NP loading and that absorption-related loss becomes significant in the near-IR, consistent with free-carrier absorption and interfacial dissipation. The Ag/PANI—10 wt.% film shows a more gradual increase in ε_i, from 0.237 at 500 nm to 0.416 at 1000 nm, 0.534 at 1500 nm, 0.861 at 2000 nm, 1.336 at 2500 nm, and 1.692 at 3000 nm. At 3000 nm, ε_i (10%) is 3.35× higher than ε_i (PANI) (1.692/0.505). The monotonic increase suggests a steadily growing loss contribution with wavelength, matching the observed increase in optical loss (k) at long wavelengths for this loading. The highest dielectric loss is achieved for Ag/PANI—15 wt.%. ε_i rises from 0.623 at 500 nm to 1.514 at 1000 nm, 2.582 at 1500 nm, 4.600 at 2000 nm, and 8.785 at 2500 nm, reaching 12.436 at 2700 nm. At 2000 nm, ε_i (15%) is 15.49× larger than PANI (4.600/0.297), demonstrating that Ag-rich films are strongly dissipative at low photon energies. At the far-right edge (≈2700–3000 nm), the ε_i curve approaches the plotted upper limit and shows oscillations; therefore, ε_i at 3000 nm is treated as not reliable for robust digitization.

This limitation is expected when k becomes large and the derivation of ε_i (Equation (10)) becomes highly sensitive to spectral noise and to the exact n–k extraction. Equations (9) and (10) rationalize why the Ag/PANI—15 wt.% film simultaneously exhibits very large ε_r and ε_i at long wavelengths: n rises strongly in the near-IR and k also increases, so ε_r ($\approx n^2$) is boosted while ε_i ($\approx 2nk$) grows even more rapidly. In contrast, the 5 wt.% film displays high ε_r and ε_i in the 2000–2500 nm region but slightly lower values at

3000 nm, consistent with a scenario where dispersion and loss peak in mid-IR/near-IR due to the particular nanoparticle distribution and carrier relaxation landscape. The 10 wt.% film shows a more moderate ε_i but a steadily increasing ε_r and ε_i toward 3000 nm, suggesting a smoother evolution of n and k with the wavelength. Overall, Figure 9 demonstrates that Ag incorporation transforms the optical dielectric response of PANI from a low-loss, weakly dispersive polymer ($\varepsilon_r \approx 2.740$–$4.110$; $\varepsilon_i \approx 0.237$–$0.505$) into a strongly dispersive and increasingly lossy nanocomposite. The strongest transformation occurs at 15 wt.% Ag, where ε_r reaches 146.119 at 3000 nm and ε_i reaches 12.436 at 2700 nm, indicating a metal-influenced, carrier-rich regime dominated by enhanced polarization and dissipation. These quantitative trends are consistent with intensified interfacial charge transfer, increased free-carrier density, and strengthened Maxwell–Wagner polarization losses as the Ag NP fraction increases [35].

3.5.2. The Dielectric Loss Tangent (*tan δ*)

Figure 8b shows the spectral evolution of the dielectric loss tangent (*tan δ*) (Equation (11)) for pristine PANI and Ag/PANI nanocomposites as a function of wavelength (≈400–3200 nm). The loss tangent is a dimensionless measure of the balance between dissipated and stored electromagnetic energy in the medium and is defined by

$$tan(\delta) = \frac{\varepsilon_i}{\varepsilon_r} \tag{11}$$

where ε_r is the real dielectric component associated with energy storage (polarization) and ε_i is the imaginary component associated with dielectric loss (dissipation). Therefore, $tan(\delta)$ increases when loss processes (ε_i) grow faster than the polarization term (ε_r), and decreases when ε_r dominates. Across the entire wavelength window, $tan(\delta)$ increases markedly with Ag NP loading, demonstrating that Ag NP incorporation introduces additional dissipation channels (e.g., interfacial polarization relaxation and carrier-related absorption) in the PANI matrix. Pristine PANI (black) exhibits the lowest loss level: $tan(\delta)$ equals 0.058 at 500 nm and increases slightly to 0.072 at 1000 nm and 0.072 at 1500 nm. In the near-IR, the loss rises further as the absorption tail becomes more important, giving $tan(\delta)$ = 0.108 at 2500 nm and 0.158 at 3000 nm. The overall increase from 500 to 3000 nm is +0.100, indicating that PANI becomes progressively more dissipative at long wavelengths, but the magnitude remains relatively modest. For Ag/PANI—5 wt.% (red), $tan(\delta)$ is higher than pristine PANI over most of the spectrum and shows a broad high-loss region in the near-IR/short-wave IR. Quantitatively, $tan(\delta)$ increases from 0.044 at 500 nm to 0.056 at 1000 nm and 0.071 at 1500 nm, then reaches 0.046 at 2000 nm and decreases to 0.029 at 2500 nm and 0.032 at 3000 nm. This behavior reflects the fact that ε_r grows strongly for 5 wt.% (large polarization storage), which can partially suppress $tan(\delta)$ even when ε_i increases [36]. In other words, the 5 wt.% composite becomes more polarizable (higher ε_r) faster than it becomes lossy (ε_i), lowering $\varepsilon_i/\varepsilon_r$ at the long-wavelength side. Ag/PANI–10 wt.% (blue) exhibits a higher loss level than 5 wt.% over a wider portion of the spectrum. The calculated $tan(\delta)$ equals 0.519 at 500 nm, decreases to 0.304 at 1000 nm and 0.234 at 1500 nm, and then remains in the 0.118–0.079 range at longer wavelengths (0.118 at 2000 nm, 0.086 at 2500 nm, and 0.079 at 3000 nm). The comparatively large value at 500 nm originates from the combination of small ε_r and finite ε_i at short wavelengths for this composition, highlighting the sensitivity of $tan(\delta)$ to the relative magnitudes of ε_i and ε_r. The highest dielectric loss is obtained for Ag/PANI—15 wt.% (green). $tan(\delta)$ equals 0.114 at 500 nm, 0.158 at 1000 nm, 0.195 at 1500 nm, 0.183 at 2000 nm, and 0.144 at 2500 nm. In the far near-IR (≈2700–3000 nm), the curve approaches the upper plotting limit and displays oscillatory behavior; therefore, $tan(\delta)$ at 3000 nm is not treated as a robust digitized value. Nevertheless, the consistently

larger $tan(\delta)$ values for the 15 wt.% film indicate that dissipation grows strongly with Ag loading, consistent with enhanced k-driven losses and a more metal-influenced optical response. Overall, the $tan(\delta)$ hierarchy across most wavelengths is Ag/PANI—15% > Ag/PANI—10% > Ag/PANI—5% > PANI, confirming that Ag nanoparticles promote dielectric loss. Because $tan(\delta)$ is defined by $\varepsilon_i/\varepsilon_r$ (Equation (11)), the observed trends reflect the coupled evolution of ε_r and ε_i: Ag NP loading increases ε_i through stronger absorption and carrier-related dissipation, while also increasing ε_r through enhanced polarization. The net $tan(\delta)$ response is governed by which term grows faster at a given wavelength, explaining why compositions with very large ε_r can show moderate $tan(\delta)$ even when ε_i is elevated [37–41].

Figure 10a–d presents the Wemple–DiDomenico (single-oscillator) analysis of the dispersion of the refractive index for pristine PANI and Ag/PANI nanocomposites through the linear representation of $(n^2 - 1)^{-1}$ as a function of $(h\nu)^2$. In this model, the refractive-index dispersion in the transparent to weakly absorbing region is described by

$$\left(n^2 - 1\right)^{-1} = \frac{E_0}{E_d} - \left(\frac{1}{E_0 E_d}\right)(h\nu)^2 \tag{12}$$

where E_0 is the single-oscillator energy and E_d is the dispersion energy, which is proportional to the strength of interband optical transitions. Equation (12) predicts a linear dependence of $(n^2 - 1)^{-1}$ on $(h\nu)^2$ with an intercept of E_0/E_d and a negative slope of $-1/(E_0E_d)$. Accordingly, the quality of the linear fit in Figure 10 indicates that the single-oscillator approximation describes the measured dispersion in the selected spectral ranges. The extracted parameters (Table 3) further yield the zero-frequency refractive index and static dielectric constant via

$$n_0 = \sqrt{1 + \frac{E_0}{E_d}} \tag{13}$$

$$\varepsilon_s = n_0^2 \tag{14}$$

together with additional derived quantities frequently used for comparative dispersion analysis [42–44]:

$$f = E_0 E_d \tag{15}$$

$$M_{-1} = \frac{E_d}{E_0} \tag{16}$$

$$M_{-3} = \frac{E_d}{E_0^3} \tag{17}$$

where f is the oscillator strength and M_{-1}, M_{-3} are spectral moments. A key outcome of Figure 10 is that all samples exhibit an approximately linear decrease of $(n^2 - 1)^{-1}$ with increasing $(h\nu)^2$, consistent with the negative slope required by Equation (12). The magnitude of the slope is controlled by $-1/(E_0E_d)$ and therefore tracks the oscillator strength f (Equation (15)): a larger f yields a smaller-magnitude slope (less steep line), while a smaller f yields a steeper line. Using the Table 3 values, the slopes are -0.1083 eV^{-2} for PANI, -0.0892 eV^{-2} for Ag/PANI—5 wt.%, -0.2165 eV^{-2} for Ag/PANI—10 wt.%, and -0.0078 eV^{-2} for Ag/PANI—15 wt.%. The 15 wt.% film therefore displays the least steep dispersion line ($|$slope$|$ reduced by 13.88× relative to PANI), reflecting its very large f = 128.21 eV^{-2}. In contrast, the 10 wt.% film has the steepest line ($|$slope$|$ = 0.2165 eV^{-2}), consistent with the smallest oscillator strength (f = 4.63 eV^{-2}) among the nanocomposites. The intercept term E_0/E_d also differs among the compositions and provides direct access to n_0 through Equation (13). From Table 3, PANI shows E_0 = 1.92 eV and E_d = 4.81 eV, giving an intercept E_0/E_d = 0.3992 and n_0 = 1.1829 (ε_s = 1.3992). Ag incorporation modifies both

E_0 and E_d. For Ag/PANI—5 wt.%, E_0 = 1.56 eV and E_d = 7.19 eV, yielding E_0/E_d = 0.2170 and n_0 = 1.1032 (ε_s = 1.2170). This indicates that although E_d increases significantly relative to pristine PANI (+49.48%), the ratio E_0/E_d decreases, leading to a reduced n_0 (−6.75% relative to PANI). For Ag/PANI—10 wt.%, E_0 = 1.79 eV and E_d = 2.58 eV, giving the largest intercept E_0/E_d = 0.6938 and thus the largest n_0 = 1.3015 (ε_s = 1.6938). This composition therefore exhibits the highest predicted static dielectric response among the reliable WDD fits, with ε_s increasing by +0.2946 relative to PANI (+21.05%). For Ag/PANI—15 wt.%, the parameters shift dramatically to E_0 = 5.27 eV and E_d = 24.30 eV, yet the ratio E_0/E_d = 0.2169 remains close to the 5 wt.% value, producing n_0 = 1.1031 and ε_s = 1.2169. Thus, the 15 wt.% sample combines an extremely large E_d with a much larger E_0, preserving a small E_0/E_d ratio and hence a modest n_0. The dispersion energy E_d is particularly informative because it reflects the average strength of interband transitions and is sensitive to bonding, coordination, and microstructure. Relative to PANI (E_d = 4.81 eV), the 5 wt.% film increases to 7.19 eV, suggesting a strengthened effective transition strength, plausibly due to enhanced electronic coupling and interfacial polarization at Ag-PANI boundaries. The 10 wt.% film decreases to 2.58 eV, indicating weaker average dispersion strength in the fitted region, which can arise from changes in morphology (e.g., porosity, dispersion state) or the redistribution of oscillator strength into loss channels captured by k rather than by the purely dispersive n term. The 15 wt.% film shows a very high E_d = 24.30 eV, consistent with a strong overall optical transition strength typical of a highly polarizable, metal-influenced composite; however, this is accompanied by a high E_0 = 5.27 eV, indicating that the effective oscillator energy shifts to higher energies.

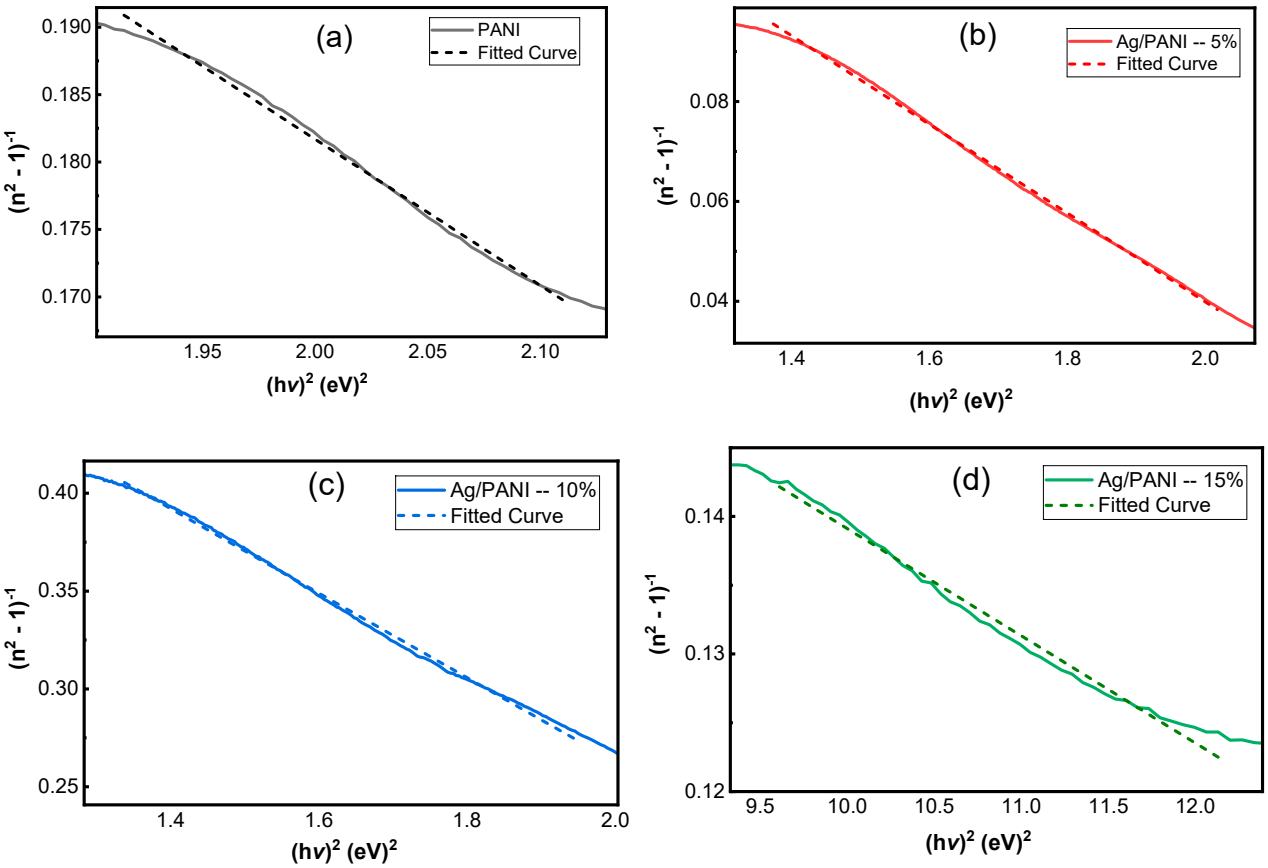


Figure 10. Plot of $(n^2 - 1)^{-1}$ versus photon energy squared ($(h\nu)^2$) for (**a**) PANI and Ag/PANI nanocomposites: (**b**) 5%, (**c**) 10%, and (**d**) 15% Ag. Experimental data and fitted lines demonstrate linear dispersion and Ag-induced modification of optical parameters.

Table 3. The values of E_d, E_0, f, n_0, ε_s, M_{-1}, and M_{-3}.

Sample	E_d (eV)	E_0 (eV)	f (eV)^2	n_0	ε_s	M_{-1} (ev)$^{-2}$	M_{-3} (ev)$^{-2}$
PANI	4.81	1.92	9.23	1.18	1.40	2.51	0.68
Ag/PANI—5 wt.%	7.19	1.56	11.25	1.10	1.22	4.60	1.88
Ag/PANI—10 wt.%	2.58	1.79	4.63	1.30	1.69	1.44	0.45
Ag/PANI—15 wt.%	24.3	5.27	128.21	1.10	1.22	4.60	0.17

The spectral moments derived further clarify these trends. $M_{-1} = E_0/E_d$ increases from 2.5052 eV^{-2} (PANI) to 4.6090 eV^{-2} (5 wt.%) and 4.6110 eV^{-2} (15 wt.%), while it drops to 1.4413 eV^{-2} at 10 wt.%. Similarly, M_{-3} increases strongly at 5 wt.% (1.8939 eV^{-2}) but becomes very small at 15 wt.% (0.1660 eV^{-2}) because of the cubic dependence on E_0 (Equation (17)). This demonstrates that the 15 wt.% sample's high E_0 suppresses M_{-3} even when E_d is very large. The oscillator strength $f = E_0E_d$ follows the order 15 wt.% (128.21) $\gg$ 5 wt.% (11.25) > PANI (9.23) > 10 wt.% (4.63), which is consistent with the relative steepness of the lines in Figure 10 via the slope term in Equation (12). Overall, Figure 10 and Table 3 show that Ag NP loading does not simply increase or decrease all dispersion parameters monotonically; rather, it reshapes the balance between oscillator energy (E_0) and dispersion energy (E_d). Moderate loading (5 wt.%) strengthens dispersion energy and oscillator strength but reduces n_0 and ε_s due to a smaller E_0/E_d ratio, whereas 10 wt.% yields the highest n_0 and ε_s because it maximizes E_0/E_d. High loading (15 wt.%) produces extremely large E_d and f with a shallow dispersion slope, consistent with a strongly polarizable composite, but retains a modest n_0 because E_0 increases concurrently. These quantitative results support the conclusion that the optical dispersion in Ag/PANI films is governed by a coupled evolution of transition strength, effective oscillator energy, and microstructure-dependent electronic coupling.

3.5.3. Nonlinear Optical Parameters

Table 4 summarizes the linear susceptibility (χ^1), the third-order nonlinear susceptibility (χ^3), and the nonlinear refractive index (n_2) for pristine PANI and Ag/PANI nanocomposites. These parameters quantify the strength of light–matter interaction in the linear and third-order nonlinear regimes and are central for evaluating the suitability of the films for nonlinear photonic applications (optical switching, limiting, and all-optical modulation). The following relations, given in Equations (18)–(22), were used to evaluate the nonlinear optical parameters from the experimentally derived optical constants. The macroscopic polarization P induced by an applied optical electric field E can be expanded as

$$P = \chi^1 E + \chi^2 E^2 + \chi^3 E^3 \tag{18}$$

where χ^1 is the linear susceptibility, χ^2 is the second-order susceptibility (often suppressed in centrosymmetric media), and χ^3 is the third-order susceptibility that governs Kerr nonlinearity and nonlinear absorption [45]. Within the Wemple–DiDomenico-based formalism used here, χ^1 and χ^3 can be related to the dispersion parameters (E_d and E_0) [46–48] by

$$\chi^1 = \frac{E_d}{4\pi E_0} \tag{19}$$

$$\chi^3 = 1.7 \times 10^{-10} \times \left(\frac{E_d}{E_0}\right)^4 \quad \text{(e.s.u.)} \tag{20}$$

Table 4. The χ^1, χ^3 and n_2 values of PANI and Ag/PANI nanocomposites.

Sample	χ^1	χ^3 (e.s.u. $\times 10^{-9}$)	n_2 (e.s.u. $\times 10^{-7}$)
PANI	0.2	6.73	2.15
Ag/PANI—5 wt.%	0.4	75.82	25.91
Ag/PANI—10 wt.%	0.1	0.73	0.21
Ag/PANI—15 wt.%	0.4	76.56	0.26

The optical refractive index can similarly be written as a field-dependent expansion:

$$n(E) = n_0 + n_1 E + n_2 E^2 + \ldots, \quad (21)$$

and the nonlinear refractive index n_2 is linked to χ^3 [49,50] through

$$n_2 = \frac{12\pi\chi^3}{n_0} \quad (22)$$

highlighting that a larger χ^3 (and smaller n_0) generally promotes stronger Kerr nonlinearity. In these equations, each parameter retains its usual optical meaning, and the set of relations was applied to obtain the composition-dependent nonlinear parameters of the Ag/PANI films. The observed U-shaped dependence of the dispersion parameters and Kerr nonlinearity suggests that the optical response is governed by a balance between Ag-induced enhancement and microstructural disruption, rather than by the filler concentration alone. At low Ag loading, an improved nanoparticle dispersion and strong Ag/PANI interfacial coupling can enhance local electromagnetic fields, interfacial polarization, and charge-transfer-assisted polarizability, leading to an increased dispersion strength and nonlinear response. At the intermediate 10 wt.% composition, partial nanoparticle aggregation and microstructural reorganization may weaken these cooperative effects by disrupting polarization continuity and reducing the efficiency of local-field enhancement, thereby producing the observed dip. Upon a further increase to 15 wt.% Ag, the larger metallic contribution appears to restore the overall polarizability and carrier-related optical response, resulting in renewed enhancement of the dispersion and Kerr-related parameters. Therefore, the non-monotonic trend reflects a competition between interfacial/local-field amplification and disorder-induced disruption within the nanocomposite structure. Pristine PANI shows χ^1 = 0.2. Incorporating Ag at 5 wt.% increases χ^1 to 0.4, i.e., a +0.2 absolute increment corresponding to a 2.00× enhancement relative to PANI. A similar χ^1 = 0.4 is obtained for the 15 wt.% nanocomposite, again 2.00× higher than pristine PANI. In contrast, Ag/PANI—10 wt.% exhibits χ^1 = 0.1, which is half the PANI value (0.50×) and indicates a reduction in the effective linear polarizability at this intermediate composition. This non-monotonic behavior suggests that χ^1 is governed not only by the Ag NP fraction but also by microstructural factors that influence the effective oscillator strength and local field distribution. The most striking effect of Ag loading is the strong amplification of χ^3 at 5 wt.% and 15 wt.%. Pristine PANI exhibits χ^3 = 6.73 × 10^{-9} e.s.u. Ag/PANI—5 wt.% increases to χ^3 = 75.82 × 10^{-9} e.s.u., which is an absolute rise of +69.09 × 10^{-9} e.s.u. and an enhancement factor of 11.27× relative to PANI. Ag/PANI—15 wt.% yields χ^3 = 76.56 × 10^{-9} e.s.u., corresponding to +69.83 × 10^{-9} e.s.u. compared with PANI and a factor of 11.38× enhancement. The 5 wt.% and 15 wt.% values are also very close to each other, differing by only 0.74 × 10^{-9} e.s.u. (≈0.98%), indicating that the system reaches a near-saturation level of χ^3 once a sufficiently strong Ag-induced electronic response and interfacial polarization are established. Conversely, Ag/PANI—10 wt.% shows a very low χ^3 = 0.73 × 10^{-9} e.s.u., which is 9.22× lower than pristine PANI and 103.9× lower than the 5 wt.% nanocomposite. Such suppression at 10 wt.% indicates that the nonlinear response is extremely sensitive to the balance between dispersion energy, oscillator energy, and

local-field enhancement; microstructural redistribution (e.g., aggregation/percolation state, disorder, or void fraction) can strongly diminish the effective third-order polarization even when the metal content is increased. The n_2 values follow the same qualitative pattern as χ^3, but with composition-dependent scaling. PANI shows $n_2 = 2.15 \times 10^{-7}$ e.s.u. A dramatic enhancement is observed for Ag/PANI—5 wt.% where $n_2 = 25.91 \times 10^{-7}$ e.s.u., i.e., $+23.76 \times 10^{-7}$ e.s.u. relative to PANI and a 12.05× increase. Ag/PANI—10 wt.% drops to $n_2 = 0.21 \times 10^{-7}$ e.s.u., which is 10.24× lower than PANI and 123.4× lower than the 5 wt.% nanocomposite. Interestingly, although Ag/PANI—15 wt.% maintains a very high χ^3 (76.56×10^{-9} e.s.u.), the reported n_2 is only 0.26×10^{-7} e.s.u., which is 8.27× lower than PANI and 99.7× lower than Ag/PANI—5 wt.%. This divergence between χ^3 and n_2 implies that the effective refractive Kerr coefficient at 15 wt.% is suppressed by additional factors embedded in Equation (22), most plausibly a large effective n_0 and/or strong competing loss/dispersion that alters the real part of the nonlinear index. In highly loaded nanocomposites, intense absorption and strong dispersion can reduce the measurable Kerr refraction and shift the nonlinear response toward absorptive contributions, even when χ^3 remains large. Overall, Table 4 demonstrates that Ag incorporation can raise χ^1 up to 0.4 and boost χ^3 to ~76×10^{-9} e.s.u., establishing strong third-order nonlinearity in the 5 wt.% and 15 wt.% nanocomposites. Among the studied compositions, Ag/PANI—5 wt.% provides the most favorable combination of a high χ^3 (75.82×10^{-9} e.s.u.) and very large n_2 (25.91×10^{-7} e.s.u.), making it the best candidate for Kerr-based nonlinear optical functionality. Because the optical constants were derived from the measured spectral response of heterogeneous films, the extracted refractive-index dispersion represents an effective optical behavior that may include contributions from morphology-related scattering in addition to true absorption. This effect is expected to be more pronounced at higher Ag loading, where AFM/SEM reveals increased roughness and aggregation; therefore, the derived dispersion and nonlinear parameters should be interpreted as effective nanocomposite optical constants rather than strictly scattering-free intrinsic values. The pronounced non-monotonic response at 10 wt.% and the $\chi^3 \mid n_2$ decoupling at 15 wt.% underscore that the nonlinear optical performance is controlled by both the composition and microstructure, including the nanoparticle dispersion state, interfacial density, and local-field factors, rather than by the filler fraction alone.

Figure 11a–d plot the real part of the dielectric constant (ε_r) as a function of the squared wavelength (λ^2) for pristine PANI and Ag/PANI nanocomposites. The ε_r (λ) values were obtained from the optical constants n and k through $\varepsilon_r = n^2 - k^2$, and the ε_r versus λ^2 representation is interpreted using the Drude-type (Spitzer–Fan) free-carrier dispersion in the infrared. In this framework, ε_r varies linearly with λ^2 as

$$\varepsilon_r = n^2 - k^2 = \varepsilon_l - \left(\frac{e^2}{4\,\pi^2 c^2 \varepsilon_0}\right)\left(\frac{N}{m^*}\right)\lambda^2 \tag{23}$$

where ε_l is the high-frequency (lattice/ionic + bound-electron) dielectric constant, e is the elementary charge, c is the speed of light, ε_0 is the permittivity of free space, and $\frac{N}{m^*}$ is the carrier concentration-to-effective-mass ratio [50,51]. Here, the terms 'free-carrier response' and 'carrier-related contribution' are used in the optical sense, based on Drude-type fitting of the dielectric-dispersion behavior and the long-wavelength evolution of the optical constants, rather than on direct electrical measurements such as dc conductivity or Hall-effect analysis. Therefore, these interpretations should be understood as optically inferred trends consistent with enhanced carrier-related polarization/loss, not as direct experimental determination of carrier density. According to Equation (23), the ε_r versus λ^2 plot should be approximately linear with (i) an intercept equal to ε_l at $\lambda^2 \to 0$ and (ii) a negative slope proportional to $\left(\frac{N}{m^*}\right)$. Thus, stronger free-carrier contributions (larger

$\left(\frac{N}{m^*}\right)$) produce a steeper decrease in ε_r with λ^2. Consistent with Equation (23), all panels in Figure 11 show a monotonic reduction in ε_r with increasing λ^2, confirming that long-wavelength dispersion is governed by carrier-related polarization rather than by a purely bound-electron response. For pristine PANI (Figure 11a), ε_r decreases smoothly across the shown λ^2 window, reflecting a weak but measurable carrier contribution. Table 5 quantifies the corresponding parameters: PANI exhibits ε_l = 8.2 and $\frac{N}{m^*}$ = 1.6 × 10^{39} (kg^{-1} m^{-3}), together with a plasma frequency ω_p = 4.8 × 10^{12} Hz. These values establish PANI as a low-carrier, weakly dispersive polymer in the present spectral range. Upon incorporating Ag, the ε_r versus λ^2 trends become markedly stronger, indicating an enhanced carrier density and/or reduced effective mass in the composite. For Ag/PANI—5 wt.% (Figure 11b), ε_r decreases almost linearly with λ^2 and the extracted bound-electron dielectric constant rises to ε_l = 193.1. Relative to PANI, this is a 23.549× increase (193.1/8.2). Simultaneously, $\frac{N}{m^*}$ increases to 27.0 × 10^{39} (kg^{-1} m^{-3}), i.e., a 16.875× enhancement over PANI (27.0/1.6). The plasma frequency rises to ω_p = 78.2 × 10^{12} Hz, which is 16.292× higher than PANI (78.2/4.8). The concurrent growth of ε_l, $\frac{N}{m^*}$, and ω_p indicates that even modest Ag loading substantially strengthens both the bound-electron polarizability and free-carrier response. Ag/PANI—10 wt.% (Figure 11c) also shows a strong ε_r versus λ^2 decrease, with parameters that remain far above pristine PANI but below the 5 wt.% and 15 wt.% extremes. Specifically, ε_l = 108.6 (13.244× PANI), $\frac{N}{m^*}$ = 21.7 × 10^{39} (13.562× PANI), and ω_p = 62.9 × 10^{12} Hz (13.104× PANI). These values demonstrate that Ag addition increases the carrier-related dispersion term in Equation (23) substantially, but the response is not strictly monotonic with loading when moving from 5 to 10 wt.%. This non-monotonicity suggests that the effective free-carrier contribution is sensitive to the microstructure, including the Ag dispersion state, percolation connectivity, and interfacial charge-transfer efficiency, rather than being determined solely by the nominal filler fraction. The most pronounced effect is observed for Ag/PANI—15 wt.% (Figure 11d). The ε_r versus λ^2 plot exhibits the steepest overall decline, consistent with the largest extracted $\left(\frac{N}{m^*}\right)$ in Table 5. Quantitatively, ε_l increases dramatically to 469.8, which is 57.293× higher than PANI. The $\left(\frac{N}{m^*}\right)$ ratio reaches 98.0 × 10^{39} (kg^{-1} m^{-3}), corresponding to a 61.250× enhancement relative to PANI. The plasma frequency increases to ω_p = 248 × 10^{12} Hz, i.e., 51.667× PANI. Because ω_p scales with carrier density (and inversely with effective mass), the very large ω_p for 15 wt.% supports a transition toward a carrier-rich, metal-influenced optical response in the near-IR, consistent with the strong increases in optical loss and dielectric loss observed in the complementary figures. From Equation (23), the slope magnitude is proportional to $\left(\frac{N}{m^*}\right)$. Therefore, comparing Table 5 provides a direct quantitative ranking of the expected slopes: |slope| (15%) > |slope| (5%) > |slope| (10%) ≫ |slope| (PANI), in agreement with the qualitative ordering of steepness in Figure 11. In addition, the substantial increase in ε_l with Ag loading (8.2 → 193.1 → 108.6 → 469.8) indicates that Ag does not only contribute free carriers; it also enhances the background polarizability (bound-electron contribution), likely through an increased electronic density of states and strong interfacial polarization at Ag/PANI boundaries. The simultaneous elevation of ε_l and $\frac{N}{m^*}$ implies that both polarization storage (intercept) and carrier dispersion (slope term) are reinforced. The relatively large ε_l values obtained for the Ag/PANI films should be interpreted with caution. In the present work, ε_l is not treated as a simple static dielectric constant of a homogeneous polymeric material, but as an effective model-derived parameter obtained from the optical dispersion analysis. Therefore, its magnitude can be strongly influenced by interfacial polarization, free-carrier contribution, structural heterogeneity, and fitting sensitivity, particularly in metal-containing nanocomposite films. From this perspective, the increase in ε_l with Ag incorporation is consistent with an enhanced polarization response within the Ag/PANI system; however, the absolute values should be regarded as

effective optical parameters within the applied model rather than direct intrinsic dielectric constants. Similar unusually high effective dielectric parameters have also been reported in heterogeneous conductive-polymer/metal and highly polarizable nanocomposite systems, where strong interface-related effects play a dominant role. Overall, Figure 11 and Table 5 confirm that Ag NP incorporation strongly amplifies the free-carrier dispersion of ε_r in PANI-based films. The high $\left(\frac{N}{m^*}\right)$ and ω_p values for Ag/PANI—15 wt.% (98.0×10^{39} and 248×10^{12} Hz) identify this composition as the most conductive/metal-like in optical dielectric behavior, while Ag/PANI—5 wt.% already exhibits a substantial enhancement ($\left(\frac{N}{m^*}\right) = 27.0 \times 10^{39}$; $\omega_p = 78.2 \times 10^{12}$ Hz) with a large $\varepsilon_l = 193.1$. The non-monotonic values at 10 wt.% highlight that the microstructure and connectivity govern the effective carrier response, and should be considered when optimizing the films for optical and optoelectronic applications requiring tailored dielectric dispersion.

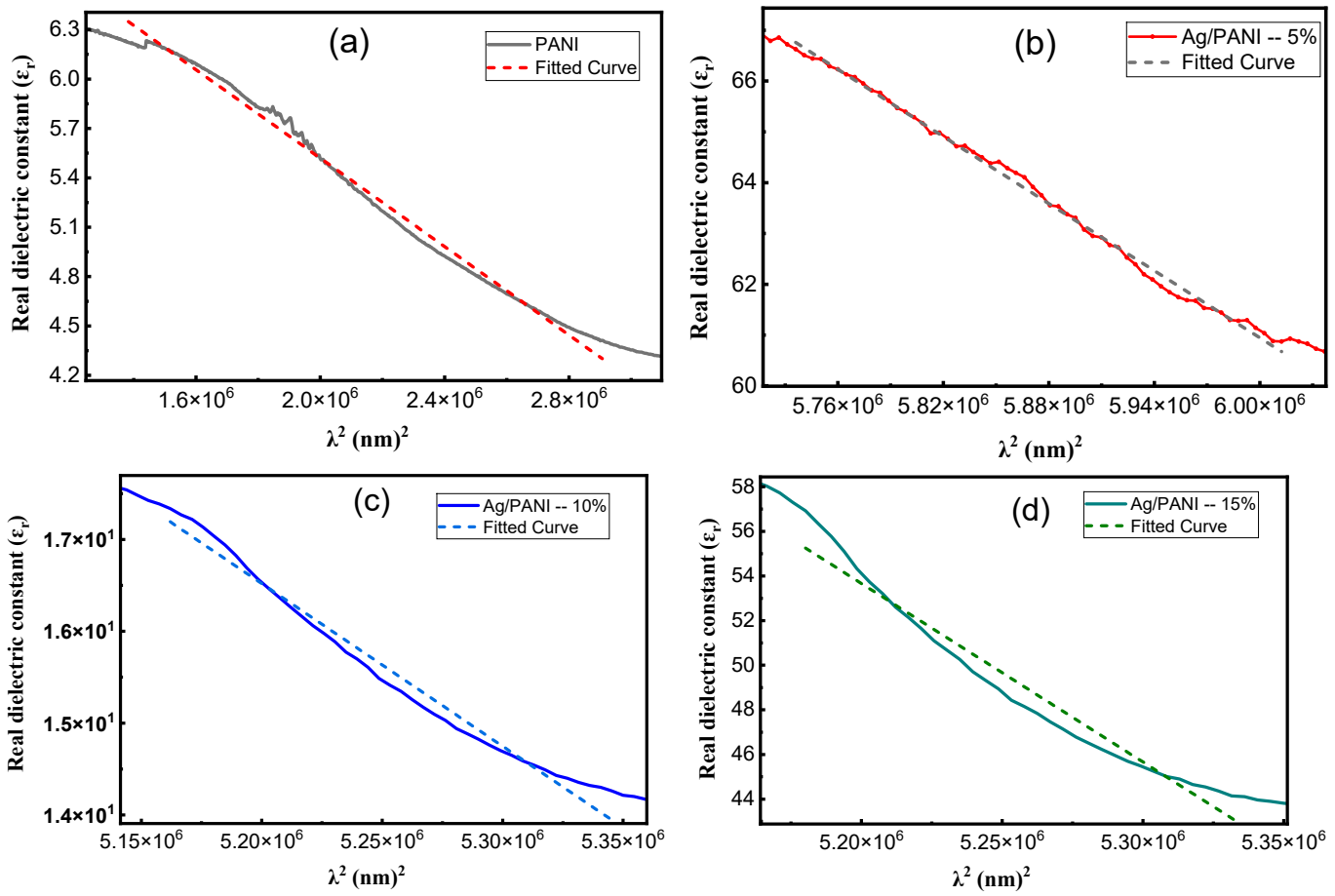


Figure 11. ε_r versus λ^2. Real dielectric constant (ε_r) versus squared wavelength (λ^2) for (**a**) PANI and Ag/PANI nanocomposites: (**b**) 5%, (**c**) 10%, and (**d**) 15% Ag. Solid curves show experimental data, and dashed curves represent fitted dispersion model results, revealing increased polarization with higher Ag loading.

Table 5. Optical parameters of PANI and Ag/PANI, including N/m^*, ε_l, ω_p, S_0, and λ_0 values.

Sample	$\frac{N}{m^*} \times 10^{39}$ ($kg^{-1}m^{-3}$)	ε_l	$\omega_p \times 10^{12}$ (Hz)	$S_0 \times 10^{-5}$ (m^{-2})	λ_0 (nm)
PANI	1.6	8.2	4.8	9.1	220
Ag/PANI—5 wt.%	27.0	193.1	78.2	0.7	790
Ag/PANI—10 wt.%	21.7	108.6	62.9	0.3	690
Ag/PANI—15 wt.%	98.0	469.8	248	4.8	440

Figure 12a–d presents the plot of $(n^2 - 1)^{-1}$ as a function of λ^{-2} for pristine PANI and Ag/PANI nanocomposites. This representation is used to evaluate normal dispersion within a single-oscillator (Sellmeier-type) approach, where the refractive index is controlled by an effective electronic resonance located at λ_0 and weighted by an oscillator strength S_0. The near-linear behavior in each panel indicates that the selected spectral range can be described by one dominant effective oscillator, allowing S_0 and λ_0 to be extracted from the linear fit. The fitting relation is

$$\left(n^2 - 1\right)^{-1} = \frac{1}{S_0 \lambda_0^2} - \left(\frac{1}{S_0}\right)\lambda^{-2} \quad (24)$$

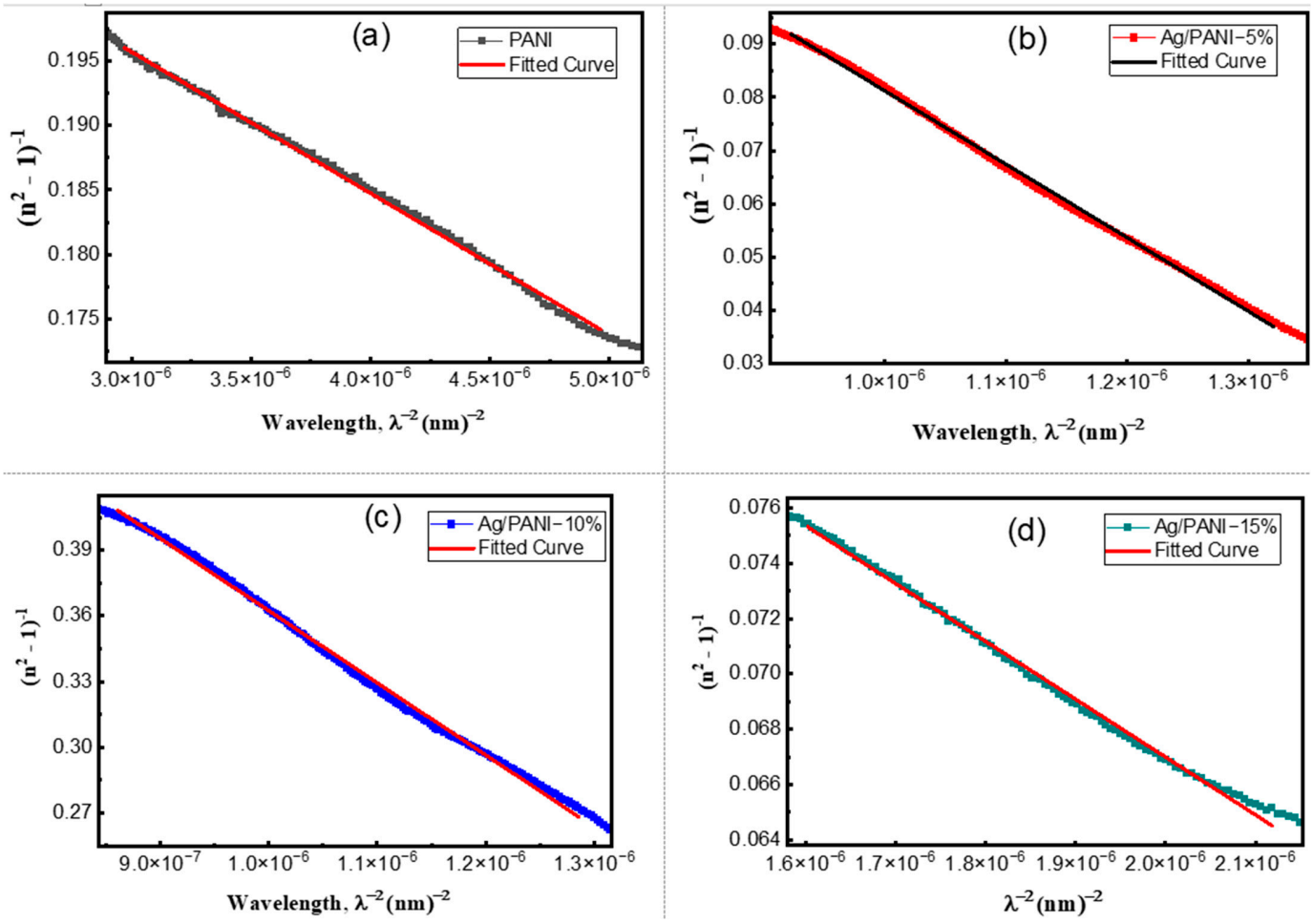


Figure 12. Plot of $(n^2 - 1)^{-1}$ versus squared wavelength (λ^2) for (**a**) PANI and Ag/PANI nanocomposites: (**b**) 5%, (**c**) 10%, and (**d**) 15% Ag. Symbols represent experimental data, and solid lines indicate linear fitting, confirming normal dispersion behavior and Ag-dependent optical response.

Equation (24) predicts a straight line with a negative slope $(-\frac{1}{S_0})$ and intercept $(\frac{1}{S_0\lambda_0^2})$. Therefore, smaller S_0 produces a larger-magnitude slope (steeper dependence on λ^{-2}), while a larger λ_0 tends to reduce the intercept for a fixed S_0. Table 5 reports the extracted S_0 and λ_0 values for all compositions. PANI exhibits $S_0 = 9.1 \times 10^{-5}$ m^{-2} and $\lambda_0 = 220$ nm. From Equation (24), these values correspond to $|-\frac{1}{S_0}| = 1.099 \times 10^4$ m^2 and an intercept $\frac{1}{S_0\lambda_0^2} = 0.2270$. The moderate slope is consistent with a polymeric matrix showing a smooth normal dispersion. The 5 wt.% composite shows a strong red-shift of the characteristic wavelength to $\lambda_0 = 790$ nm (3.5909× PANI) together with a sharp reduction in oscillator strength to $S_0 = 0.7 \times 10^{-5}$ m^{-2} (0.0769× PANI). Consequently, the

slope magnitude increases to $|-\frac{1}{S_0}| = 1.4286 \times 10^5$ m^2, which is 13.00× higher than PANI. Notably, the intercept remains close to the PANI value (0.2289 versus 0.2270), changing by only +0.0019 (+0.82%), because the decrease in S_0 is largely compensated by the increase in λ_0^2 in the intercept term. The 10 wt.% film exhibits the smallest oscillator strength, $S_0 = 0.3 \times 10^{-5}$ m^{-2} (0.0330× PANI), and a large $\lambda_0 = 690$ nm (3.1364× PANI). This combination yields the steepest dispersion line in the series, with $|-\frac{1}{S_0}| = 3.3333 \times 10^5$ m^2 (30.33× PANI). In addition, the intercept rises markedly to 0.7001, i.e., 3.08× PANI, indicating that the reduction in S_0 is not fully offset by λ_0^2 for this composition. The 10 wt.% sample therefore displays the strongest effective dispersion within the Equation (24) fit, consistent with its exceptionally large $|-\frac{1}{S_0}|$ value. At 15 wt.% Ag, S_0 increases to 4.8×10^{-5} m^{-2} (0.5275× PANI) while λ_0 decreases to 440 nm (2.000× PANI). As a result, the slope magnitude drops to $|-\frac{1}{S_0}| = 2.0833 \times 10^4$ m^2, only 1.8958× higher than PANI and far smaller than the 5 and 10 wt.% cases.

The intercept decreases to 0.1076, which is 0.474× the PANI value. This indicates that high Ag loading partially restores the effective oscillator strength (larger S_0), reducing the steepness of the λ^{-2} dispersion, while maintaining a resonance shifted to longer wavelengths than pristine PANI. The extracted λ_0 values evolve non-monotonically with Ag NP loading: 220 nm (PANI) → 790 nm (5 wt.%) → 690 nm (10 wt.%) → 440 nm (15 wt.%). This signifies a pronounced red-shift of the effective dispersion resonance at intermediate loadings, followed by a partial blue-shift at the highest loading. In parallel, S_0 decreases strongly at 5 wt.% (−92.31% relative to PANI) and 10 wt.% (−96.70%), then increases at 15 wt.% (4.8×10^{-5} m^{-2}) but remains below PANI (−47.25%). Since the slope equals $-\frac{1}{S_0}$, these values explain the steepness ranking directly: 10 wt.% (steepest) > 5 wt.% ≫ 15 wt.% > PANI. Overall, Figure 12 and Table 5 demonstrate that Ag addition tunes the dispersion behavior by jointly altering oscillator strength (S_0) and resonance position (λ_0). The strong S_0 suppression at 5–10 wt.% implies that the effective single-oscillator contribution becomes weaker, even while λ_0 shifts to much longer wavelengths, consistent with Ag-induced electronic coupling and interfacial polarization effects. At 15 wt.%, the recovery of S_0 together with a smaller λ_0 suggests a change in the electronic environment and connectivity (e.g., stronger metal-like interaction and altered percolation), leading to a less steep but still Ag-modified dispersion response.

3.6. FTIR Spectra

Figure 13 shows the FTIR absorbance spectra of pristine PANI and Ag/PANI nanocomposite films (5, 10, and 15 wt.% Ag) collected over the 4000–400 cm^{-1} range. Presenting the spectra in absorbance highlights the evolution of vibrational band intensities with Ag incorporation, where larger peak heights correspond to stronger infrared absorption. The labeled wavenumbers (3777, 3194, 2970, 2357, 1730, 1593, 1386, 1143, 1026, 778, 589, and 516 cm^{-1}) provide a quantitative guide for band assignment and compositional comparison. In the high-wavenumber region, the weak feature at 3777 cm^{-1} is consistent with O–H stretching from surface hydroxyl groups or weakly bound moisture. The broad band centered around 3194 cm^{-1} is characteristic of N–H stretching in PANI (amine/imine units), typically broadened by hydrogen bonding. Compared with pristine PANI, the Ag/PANI spectra show this region as a smoother baseline with a reduced fine structure, suggesting that Ag addition modifies the local hydrogen-bonding environment and the effective dipole-moment change in N–H vibrations. A smaller contribution near 2970 cm^{-1} is attributable to C–H stretching (aliphatic/aryl), which can include residual organic species from processing [52]. The distinct band around 2357 cm^{-1} is commonly associated with atmospheric CO_2 absorption (asymmetric stretching). Its presence across the spectra is therefore treated as an external contribution rather than a chemical fingerprint of the films.

In the carbonyl region, the absorption at 1730 cm^{-1} indicates a C=O stretching component. In PANI-based systems, this can arise from minor oxidative functionalities, residual dopant/solvent-derived groups, or interfacial species generated during film growth. The emergence of a measurable 1730 cm^{-1} contribution in the Ag/PANI films suggests that Ag incorporation increases the population or IR activity of carbonyl-type groups, consistent with a more reactive interfacial environment [53].

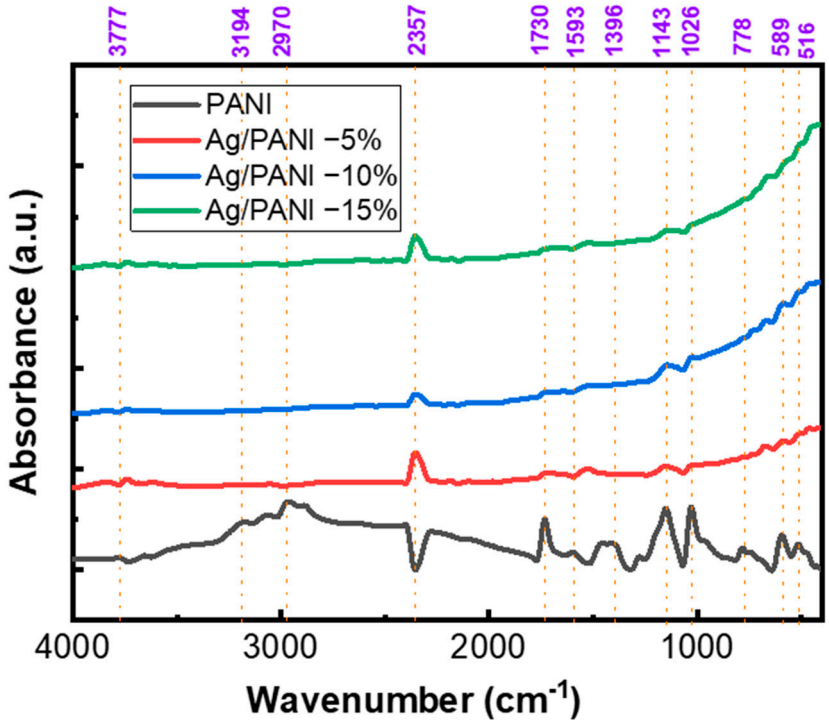


Figure 13. FTIR absorbance spectra of pristine PANI and Ag/PANI. Characteristic bands at 3777, 3194, 2970, 2357, 1730, 1593, 1386, 1143, 1026, 778, 589, and 516 cm^{-1} highlight O-H/N–H stretching, backbone ring and C-N vibrations, doped-state sensitive modes, and low-frequency interfacial features that evolve with Ag loading.

The aromatic backbone region provides the primary evidence that the PANI structure is retained in the nanocomposites. The band at 1593 cm^{-1} lies within the range of quinoid/benzenoid ring stretching vibrations in PANI. Changes in the intensity and sharpness of this feature with Ag loading indicate altered conjugation and chain packing. The band at 1386 cm^{-1} is consistent with C–N stretching and/or ring deformation modes; in doped PANI, this region can also be influenced by counter-ion interactions, so its persistence supports that the polymer remains in a doped/protonated form [54]. A prominent absorption at 1143 cm^{-1} is widely recognized in doped PANI as an "electronic-like" band associated with C–N^+ stretching coupled to charge delocalization (polaron/bipolaron states). The clear presence of the 1143 cm^{-1} band in the Ag/PANI spectra indicates that Ag incorporation does not suppress the conducting-state vibrational signature; rather, it can enhance local polarization and charge-transfer coupling at the Ag–PANI interface. The neighboring feature at 1026 cm^{-1} is attributed to in-plane C–H bending and/or C–N stretching contributions; variations in this band are sensitive to dopant configuration and local chain conformation, providing further evidence that Ag affects the polymer–dopant microenvironment [55]. In the low-wavenumber region, the band at 778 cm^{-1} corresponds to out-of-plane aromatic C–H deformation, while the features at 589 and 516 cm^{-1} are assigned to ring deformation modes and/or interfacial vibrations involving metal–nitrogen coordination or metal-oxide/hydroxide surface layers on Ag NPs. The presence and

strengthening of these low-frequency bands in the composites is consistent with additional vibrational contributions introduced by the nanoparticle phase and its interface with the polymer matrix [56]. Overall, the spectra confirm that (***i***) the PANI backbone vibrations remain present after Ag incorporation (retention of the 1593, 1386, 1143, and 1026 cm^{-1} regions), and (***ii***) Ag NP loading modifies the spectral envelope and relative band intensities, especially in the doped-state sensitive band at 1143 cm^{-1} and the low-frequency region (589–516 cm^{-1}). The systematic labeling of peaks at 3777, 3194, 2970, 2357, 1730, 1593, 1386, 1143, 1026, 778, 589, and 516 cm^{-1} provides direct quantitative markers for tracking compositional trends and supports the conclusion that Ag nanoparticles introduce stronger interfacial interactions and enhanced local polarization within Ag/PANI nanocomposite films [57–60].

3.7. Electrical Conductivity

Electrical (DC) conductivity was measured for pristine polyaniline (PANI) and Ag/PANI nanocomposites. The measured conductivities reveal a systematic enhancement of charge transport upon incorporation of Ag nanoparticles, indicating that metallic inclusions and polymer–metal interfacial coupling effectively strengthen the conductive network within the film. Pristine PANI exhibits a baseline conductivity of σ = 1.0 S·cm^{-1}. This value reflects charge transport dominated by polaron/bipolaron carriers along conjugated segments with interchain hopping across disordered regions. The moderate conductivity of the polymer matrix sets the reference for evaluating the impact of Ag loading. Upon adding 5 wt.% Ag, conductivity increases to σ = 2.6 S·cm^{-1}. This corresponds to a 2.60× enhancement relative to pristine PANI and an absolute gain of $\Delta\sigma$ = +1.6 S·cm^{-1} (i.e., a +160% increase). At this loading, Ag nanoparticles are expected to introduce additional conductive islands and locally enhance carrier mobility by strengthening chain packing and facilitating charge transfer at Ag-PANI interfaces. Even if a fully continuous Ag-Ag percolation path is not yet formed, the reduced effective hopping distance between conducting domains can substantially decrease the overall resistance. Further increasing Ag to 10 wt.% yields σ = 4.2 S·cm^{-1}, representing a 4.20× enhancement and $\Delta\sigma$ = +3.2 S·cm^{-1} (+320%) compared with PANI. Relative to the 5 wt.% film, conductivity rises by 1.6 S·cm^{-1} (from 2.6 to 4.2 S·cm^{-1}), indicating that the increased nanoparticle population promotes improved connectivity among conductive regions. This behavior is consistent with the development of more frequent interparticle junctions and a higher density of polymer–metal interfaces, both of which facilitate current flow across the film plane. The highest Ag loading (15 wt.%) produces the maximum conductivity, σ = 7.0 S·cm^{-1}. This corresponds to 7.00× the PANI value, with $\Delta\sigma$ = +6.0 S·cm^{-1} (+600%). Compared with the 10 wt.% film, σ increases by 2.8 S·cm^{-1} (from 4.2 to 7.0 S·cm^{-1}), which is a +66.7% increment. The stronger rise between 10 and 15 wt.% suggests that the composite approaches a more effective percolative transport regime, where Ag-assisted pathways contribute more directly to DC conduction. In this regime, current is expected to propagate through a hybrid network consisting of conducting PANI domains bridged by closely spaced Ag NPs, reducing the dominance of hopping-limited polymer transport. From an electrical-transport standpoint, the monotonic increase in σ across 0–15 wt.% Ag indicates that, within the investigated range, the benefits of increased connectivity and interfacial charge-transfer outweigh possible adverse effects such as nanoparticle agglomeration or junction barrier formation. Nevertheless, the absolute conductivity remains below that of bulk metals, confirming that the films behave as polymer-dominated composites rather than continuous metallic layers. Overall, the Ag/PANI nanocomposites demonstrate a clear improvement in DC conductivity with Ag incorporation: 2.6 S·cm^{-1} (5 wt.%), 4.2 S·cm^{-1} (10 wt.%), and 7.0 S·cm^{-1} (15 wt.%) compared with 1.0 S·cm^{-1} for pristine PANI. These results indicate that controlling Ag loading

is an effective route to tune electrical transport in PANI-based thin films for applications requiring enhanced conductivity.

3.8. Surface Morphology

The pristine PANI film (Figure 14a) exhibits a distinctly anisotropic, fibrous/lamellar texture, with elongated features arranged in partially aligned bundles. This morphology is consistent with electro-polymerization dominated by directional growth and coalescence of polymer domains, yielding a surface with pronounced micro-scale ridges and inter-fiber gaps. Such a structure typically provides a relatively high external surface area while maintaining a continuous polymer network, which is beneficial for electronic conduction along interconnected pathways. Upon introducing a low-Ag NP fraction (Figure 14b), the surface becomes more heterogeneous and less uniformly fibrillar. The micrograph indicates the development of fine granular contrast superimposed on the polymer background, suggesting that Ag NPs (and/or NP-rich domains) are embedded within or anchored onto the PANI matrix. At this loading, the polymer still appears to form a continuous scaffold, while the nanoparticles plausibly increase nucleation density and disrupt long-range fiber alignment. The overall morphology suggests a transition from purely polymer-controlled growth to composite-assisted nucleation, without severe clustering. At intermediate loading (Figure 14c), the surface evolves toward a more densely textured and particulate-rich appearance. Compared with 5 wt.%, the microstructure shows larger aggregated features and a more pronounced "clustered" topography, indicating that nanoparticle–nanoparticle interactions increasingly compete with polymer encapsulation. This regime typically corresponds to a morphology where the polymer matrix still bridges domains, but the surface becomes dominated by composite nodules and a higher density of protrusions, which can increase the effective area yet also introduce stronger spatial variations in local conductivity and interfacial potential. At the highest Ag content (Figure 14d), the film displays the most irregular and defect-prone surface, with conspicuous heterogeneity and features consistent with agglomeration and nonuniform coalescence. The polymer texture appears less clearly fibrous and more disrupted, implying that excessive particle content can hinder uniform polymer growth and promote stress accumulation during deposition and drying. This morphology can create mixed outcomes: it may increase surface roughness and potential active sites, but it can also reduce film uniformity and continuity, promoting microvoids or weakly connected domains that adversely affect reproducibility and long-term stability.

The SEM series supports a coherent mechanism in which Ag NPs initially act as additional nucleation/anchoring sites within the growing PANI, leading to moderated disruption of polymer alignment (5 wt.%). As loading increases (10–15 wt.%), particle–particle interactions become more influential, favoring cluster formation and a more heterogeneous composite texture. This progression is important because it directly affects interfacial and transport behavior. First, rough, clustered surfaces typically provide a higher density of accessible sites, which can enhance interfacial processes.

However, excessive clustering may compromise transport uniformity and percolation by producing spatially nonuniform conduction pathways and localized barriers, particularly if polymer bridging becomes insufficient. Second, highly heterogeneous growth can concentrate stress, and thereby weaken film cohesion and disrupt continuity. Overall, SEM confirms that Ag incorporation does not merely "decorate" the PANI surface; rather, it restructures the growth morphology in a loading-dependent manner. These microstructural findings provide a critical basis for correlating the Ag content with the film's functional properties in later sections [61,62].

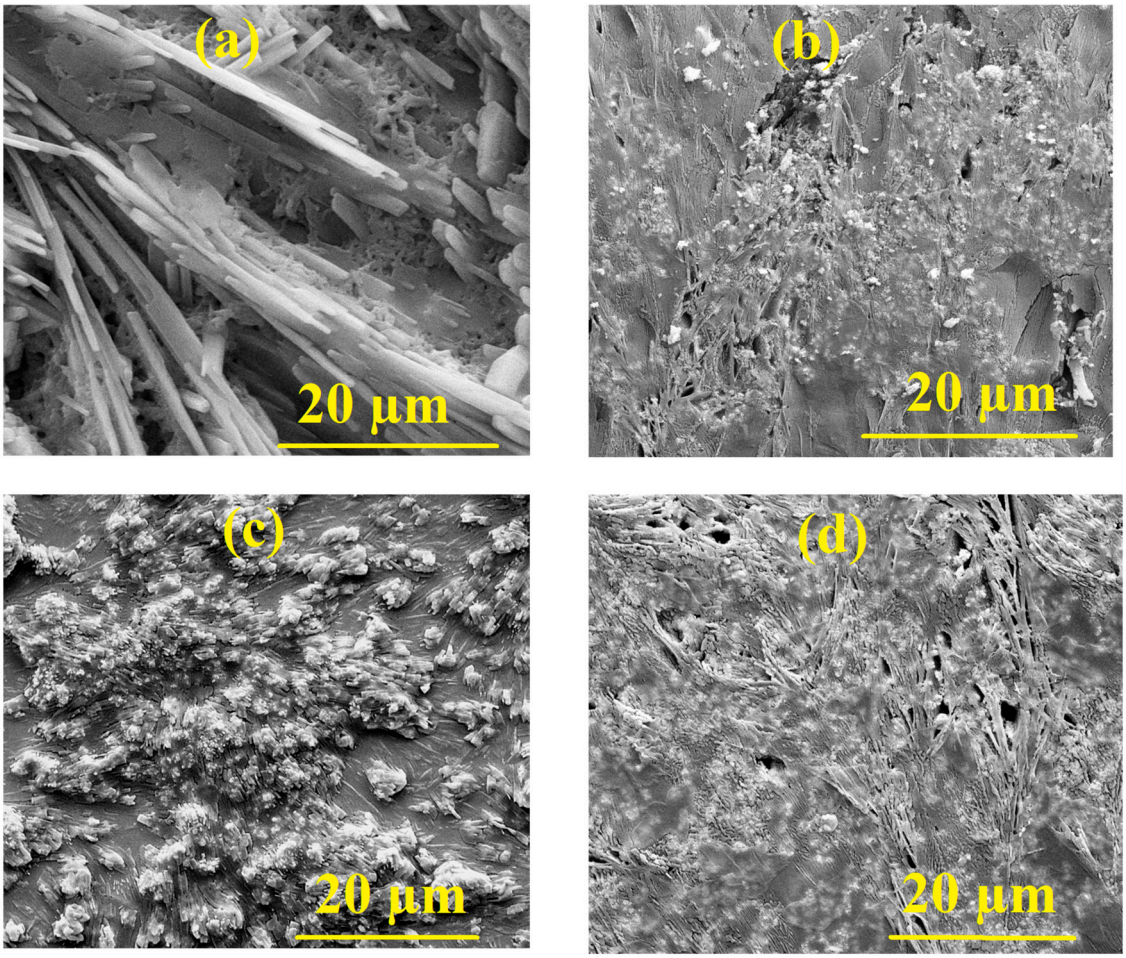


Figure 14. SEM micrographs of electrochemically deposited PANI and Ag/PANI films with increasing Ag NP content: (**a**) pristine PANI (fibrous/lamellar), (**b**) 5 wt.% Ag/PANI (granular, more heterogeneous), (**c**) 10 wt.% Ag/PANI (denser particulate/nodular), and (**d**) 15 wt.% Ag/PANI (highest heterogeneity/agglomeration). All images are at the same magnification (scale bar: 20 µm).

3.9. XRD Analysis

The pristine PANI film exhibits a semi-crystalline fingerprint consisting of broad reflections at 2θ = 9.29°, 15.63°, 18.28°, 22.56°, and 27.43°(Figure 15). These features are commonly associated with short-range ordering of the emeraldine salt form of PANI and periodic packing of polymer chains. Using Cu K_α radiation (λ = 1.5406 Å), the corresponding interplanar spacings are d = 9.513, 5.665, 4.848, 3.938, and 3.250 Å, respectively (Table A2). The reflections centered near ~18–23° can be indexed to the (110) and (200) family reported for partially ordered PANI domains; in the present film, the (110)-type peak at 2θ = 18.28° exhibits FWHM = 0.115° (Scherrer D ≈ 73.3 nm), while the (200)-type peak at 2θ = 22.56° has FWHM = 0.136° (D ≈ 62.3 nm). The breadth of these peaks confirms that ordering is limited to nanoscale coherence lengths rather than long-range crystallinity. Upon incorporating Ag nanoparticles, the PANI-related features remain present but undergo subtle shifts and broadening changes, indicating that metal loading perturbs chain packing and inter-chain spacing. In addition, distinct Bragg peaks emerge at 2θ = 38.63–38.78° and 44.82–44.97°, which are assigned to the (111) and (200) reflections of face-centered cubic (fcc) metallic Ag. The measured d-spacings for Ag (111) decrease slightly from 2.329 Å (5 wt.% Ag, 2θ = 38.63°) to 2.320 Å (15 wt.% Ag, 2θ = 38.78°), consistent with a small lattice contraction or interfacial strain within the polymer matrix. From these reflections, the corresponding fcc lattice parameter is a ≈ 4.02–4.04 Å (calculated from d111$\sqrt{3}$ and

2d200), which is close to the bulk value expected for Ag and supports the metallic phase assignment. The Ag peaks become more evident with increasing Ag loading, while no additional reflections attributable to silver oxides are apparent within the detection limit of the plotted data, suggesting that the deposited nanoparticles are predominantly metallic. Line-broadening analysis further indicates that Ag is present as nanocrystalline domains. For the Ag (111) peak, the extracted FWHM values are 0.196°, 0.189°, and 0.170° for 5, 10, and 15 wt.% Ag, corresponding to Scherrer crystallite sizes of 45.1, 46.5, and 51.8 nm, respectively. Within the uncertainty of plot-based digitization, these values indicate an Ag crystallite size in the order of ~10 nm across the composition window, with peak sharpening and intensity growth primarily reflecting a higher phase fraction and improved diffracting volume rather than a dramatic change in size. Meanwhile, the PANI (110)/(200) peaks show composition-dependent shifts (e.g., the (200)-type peak moves from 22.56° in PANI/low-Ag films to 22.85° at 15 wt.% Ag), consistent with modest contraction of the average inter-chain spacing (d decreases from 3.938 to 3.888 Å). Overall, the XRD results confirm the successful incorporation of fcc Ag nanoparticles into the PANI matrix while preserving the polymer's semi-crystalline signature.

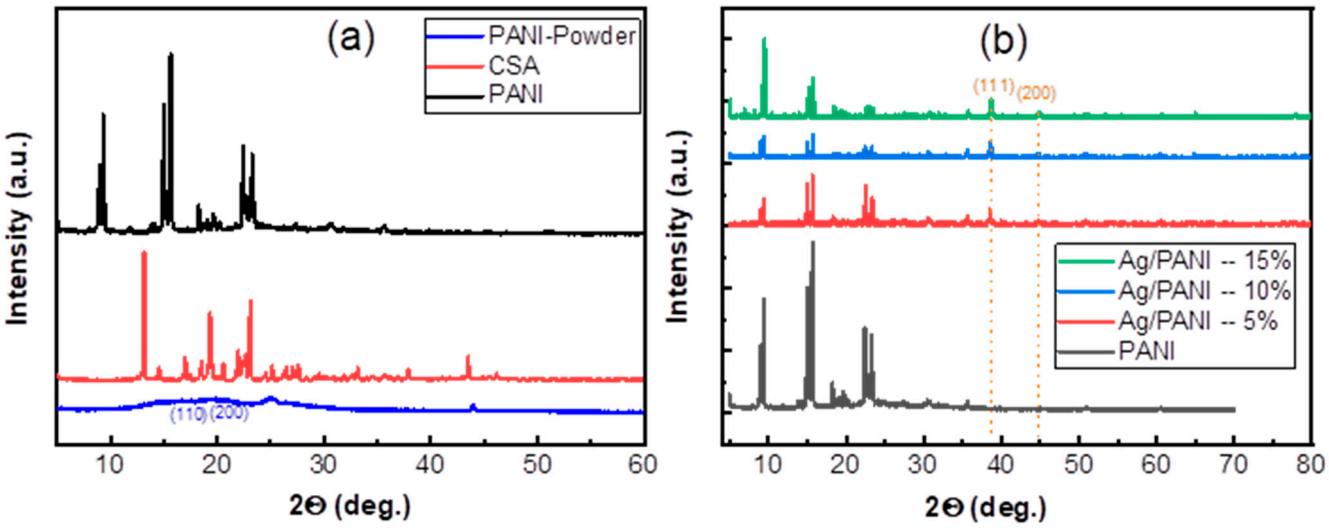


Figure 15. XRD patterns of (**a**) PANI, CSA, and PANI powder, and (**b**) pure PANI and Ag/PANI nanocomposite films with 5, 10, and 15 wt.% Ag. The Ag/PANI films show the emergence and growth of the fcc Ag peaks at $2\theta \approx 38.1°$ and 44.3°, assigned to the (111) and (200) planes, confirming successful Ag incorporation into the PANI matrix.

Williamson–Hall (W–H) Microstructural Analysis

The crystallographic broadening of diffraction peaks in semicrystalline conducting polymers and their metal–polymer nanocomposites is commonly governed by the combined effects of a finite coherent domain size and lattice distortions (microstrain). To separate these two contributions for the present thin films, the Williamson–Hall (W–H) approach was employed using the uniform deformation model. The analysis is based on the linearized relation:

$$\beta_s \ cos(\theta) = \varepsilon \ (4 \ sin(\theta)) + \frac{K\lambda}{D} \quad (25)$$

where β is the full width at half maximum (FWHM) expressed in radians after converting from degrees, θ is the Bragg angle, K is the Scherrer shape factor, λ is the X-ray wavelength (Cu Kα), D is the average crystalline grain size (coherent domain size), and ε is the microstrain. Accordingly, a plot of $\beta \ cos(\theta)$ versus 4 $sin(\theta)$ yields a straight line whose intercept equals $K\lambda/D$ (allowing extraction of D) and whose slope corresponds to the microstrain ε

(Figure 16). The resulting microstructural parameters for pristine PANI and Ag/PANI films with 5–15 wt.% Ag are summarized in Table 6. For pristine PANI, W–H fitting gives an average crystalline grain size of D = 58 nm together with a microstrain of $\varepsilon = 6.47 \times 10^{-4}$. The corresponding dislocation density, estimated from the usual inverse-square dependence on crystallite size ($\delta \approx 1/D^2$), is $\delta = 29.7 \times 10^{13}$ m^{-2}, indicating a comparatively defect-rich microstructure typical of electrochemically grown PANI where chain packing is locally disrupted by dopant counter-ions and polymerization-induced disorder. Upon incorporation of Ag NPs, the coherent domain size increases markedly. At 5 wt.%, D rises to 69 nm, while at 10 wt.% and 15 wt.%, it reaches 91 nm and 92 nm, respectively. This monotonic increase in D with Ag NP loading indicates that Ag NP incorporation promotes improved structural coherence of the PANI matrix, plausibly by facilitating more effective chain organization and by reducing the density of size-limiting defects through heterogeneous nucleation and enhanced local ordering around the metallic inclusions.

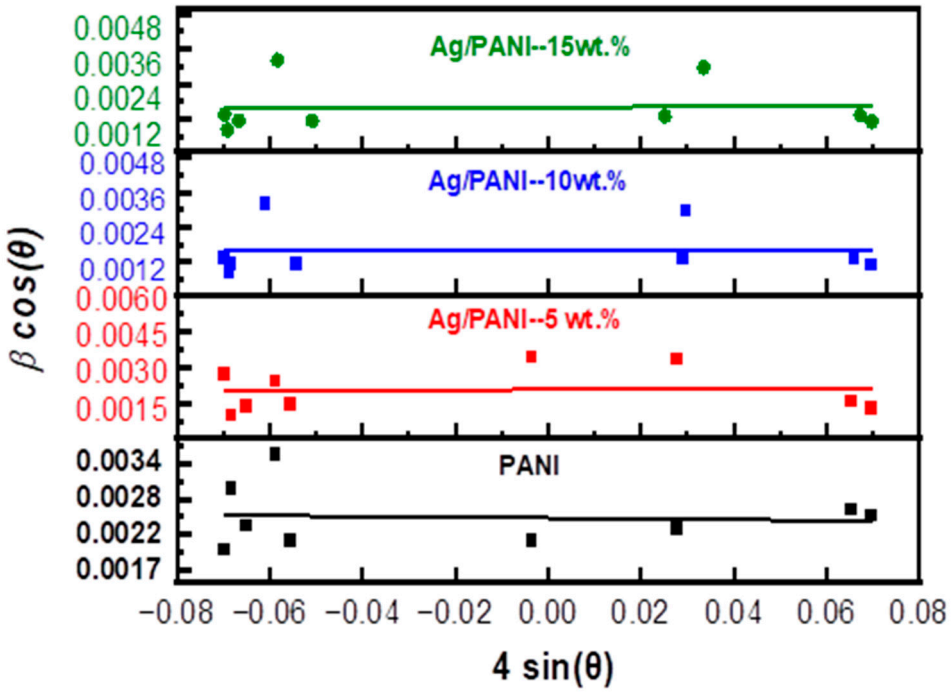


Figure 16. W-H plot of PANI and Ag/PANI nanocomposites.

Table 6. Extracted crystallographic features of PANI-based nanocomposites, including crystallite size, dislocation density, lattice strain, and strain energy density.

Sample	Average Crystalline Grain Size (D) (nm)	Strain ($\varepsilon \times 10^{-4}$)	Dislocation Density ($\delta \times 10^{13}$ m^{-2})	Strain Energy Density (U_s) (J/m^3) [62,63]
PANI	58	6.47	29.7	5.23×10^2
Ag/PANI—5 wt.%	69	10.8	21.9	1.46×10^3
Ag/PANI—10 wt.%	91	2.8	12.2	9.80×10^1
Ag/PANI—15 wt.%	92	5.6	12.1	3.92×10^2

In contrast to the steady grain-growth trend, the lattice strain exhibits a non-monotonic dependence on Ag content, reflecting the competing roles of interfacial mismatch and strain relaxation through coarsening. Specifically, the microstrain increases from 6.47×10^{-4} (PANI) to 10.8×10^{-4} at 5 wt.%, suggesting that initial Ag insertion introduces localized stress fields at Ag/PANI interfaces and/or perturbs the polymer lattice through mismatch in thermal/elastic response. At higher loading, however, the strain relaxes strongly: ε decreases to 2.8×10^{-4} at 10 wt.%, the lowest value among all samples, before rising

moderately to 5.6×10^{-4} at 15 wt.%. The minimum strain at 10 wt.% indicates that this composition achieves the most relaxed microstructure, where the benefits of increased coherence length and improved packing outweigh the strain introduced by additional interfaces. The slight re-increase at 15 wt.% can be attributed to the higher interfacial area and possible nanoparticle–nanoparticle proximity effects, which may reintroduce lattice distortions even though D remains high. Consistent with the grain-size evolution, the dislocation density decreases substantially with Ag NP addition. δ decreases from 29.7×10^{13} m^{-2} for PANI to 21.9×10^{13} m^{-2} at 5 wt.% and reaches 12.2×10^{13} m^{-2} and 12.1×10^{13} m^{-2} at 10 and 15 wt.%, respectively. The nearly identical δ values for 10 and 15 wt.%, together with the saturation of D near ~92 nm, suggest that the defect suppression and ordering improvement approach a plateau beyond ~10 wt.%. In other words, once a sufficiently coherent polymer–metal network is established, further Ag incorporation contributes less to increasing the coherent domain size and mainly modulates strain through interfacial effects.

To further link macrostrain to stored elastic energy, the strain energy density was estimated using the commonly adopted expression (Equation (26)) [62,63].

$$U_s = 1/2\ E\ \varepsilon^2 \tag{26}$$

where E is Young's modulus and ε is the microstrain in absolute units. Using E = 2.5 GPa as a representative modulus for PANI-based films, the calculated strain energy densities are $U_s = 5.233 \times 10^{+2}$ J/m^3 (PANI), $1.458 \times 10^{+2}$ J/m^3 (5 wt.%), $9.800 \times 10^{+1}$ J/m^3 (10 wt.%), and $3.920 \times 10^{+2}$ J/m^3 (15 wt.%). The U_s trend follows the strain evolution: the highest energy at 5 wt.% reflects the elevated microstrain, whereas the minimum at 10 wt.% confirms this film as the most strain-relaxed despite its large grain size. The moderate increase at 15 wt.% again highlights the contribution of interfacial strain as Ag loading rises.

Overall, the W–H analysis demonstrates that Ag NP incorporation significantly enhances crystalline coherence in PANI thin films (D increases from 58 nm to ~92 nm) and suppresses defect density (δ decreases from 29.7×10^{13} m^{-2} to 12.1×10^{13} m^{-2}). Meanwhile, microstrain and the associated elastic energy display a non-monotonic response with a pronounced optimum at 10 wt.%, where the film combines a large coherent domain size with the lowest microstrain and stored energy. These microstructural outcomes are consistent with a transition from interface-dominated distortions at low Ag loading to strain-accommodated, structurally stabilized nanocomposite films at intermediate loading, followed by renewed interfacial distortion at the highest Ag NP fraction.

Table 7 highlights that the Ag filled PANI films in this work behave very differently from previously reported PANI/oxide nanocomposites. Here, Ag incorporation drives a strong reduction in the indirect bandgap from 1.98 eV (PANI) to 1.81 eV (5 wt.% Ag), 1.38 eV (10 wt.% Ag), and 1.19 eV (15 wt.% Ag), placing the system in a distinctly low-gap regime. In contrast, oxide-filled PANI systems (NiO, TiO_2, $NiFe_2O_4$, Al_2O_3) show much larger gaps of 3.45–3.79 eV, consistent with the wide-bandgap nature of these fillers and stronger carrier localization. The Urbach energy in this work increases sharply from 377 meV to 1280–1640 meV at 5–10 wt.% Ag, indicating broad tail states and enhanced energetic disorder; by comparison, oxide composites exhibit relatively low EU (220–470 meV). Structurally, the strain in Ag/PANI is non-monotonic ($10.8 \times 10^{-4} \rightarrow 2.8 \times 10^{-4} \rightarrow 5.6 \times 10^{-4}$), suggesting competing interfacial distortion and relaxation, whereas oxide systems mostly remain within the ~10^{-4} range.

Table 7. Optical and structural parameters of PANI and its nanocomposites: This work versus selected published studies.

Sample	Ref.	Indirect Energy Gap (E_g) (eV)	Urbach Energy (meV)	Strain (ε)
PANI	This work	1.98	377	6.47×10^{-4}
Ag/PANI—5 wt.%	This work	1.81	1280	10.8×10^{-4}
Ag/PANI—10 wt.%	This work	1.38	1640	2.8×10^{-4}
Ag/PANI—15 wt.%	This work	1.19	Not reliable	5.6×10^{-4}
PANI/NiO—5 wt.%	[64]	3.45	290	13.5×10^{-4}
PANI/TiO_2—10 wt.%	[64]	3.53	240	5.90×10^{-4}
PANI/$NiFe_2O_4$—15 wt.%	[65]	3.60	220	5.00×10^{-4}
PANI/Al_2O_3—5 wt.%	[56]	3.76	463	3.6×10^{-4}
PANI/Al_2O_3_10 wt.%	[56]	3.79	470	4.9×10^{-5}

4. Conclusions

This work establishes a composition-resolved understanding of how Ag NPs restructure the electronic and optical response of electrodeposited PANI thin films on ITO, addressing a persistent gap in the literature where band-edge disorder, dispersion energetics, dielectric carrier effects, and χ^3 are typically treated separately. Using a single, controllable fabrication route (potentiostatic electrodeposition with 5–15 wt.% Ag in the electrolyte), the films provide a consistent platform to isolate loading-dependent trends relevant to integrated optoelectronics. Key outcomes can be summarized as follows. (***i***) Electronic-structure tuning is accompanied by strong disorder broadening: Ag addition narrows the indirect gap from 1.98 eV (pristine PANI) to 1.81, 1.38, and 1.19 eV at 5, 10, and 15 wt.% Ag, respectively, while the Urbach energy rises sharply to 1.28–1.64 eV at 5–10 wt.%, indicating a substantial increase in localized tail states and electron–phonon coupling signatures (with Urbach fitting becoming unreliable at 15 wt.% under strong loss conditions). (***ii***) Dispersion parameters evolve non-monotonically, revealing that the Ag fraction alone is not predictive: the Wemple–DiDomenico analysis shows that the dispersion energy and oscillator energy shift in different directions across the series, consistent with competing effects of interfacial polarization, morphology, and redistribution of oscillator strength. (***iii***) The dielectric response transitions toward a carrier-rich regime at high loading: Drude-type analysis indicates large increases in ε_∞, N/m*, and ω_p, reaching $\varepsilon_\infty \approx 469.8$ and $\omega_p \approx 248 \times 10^{12}$ Hz for 15 wt.% Ag, evidencing pronounced long-wavelength polarization and free-carrier contributions. (***iv***) Third-order nonlinearity is strongly enhanced yet highly sensitive to the microstructure: χ^3 increases by more than an order of magnitude at 5 and 15 wt.% ($\approx 7.6 \times 10^{-8}$ esu), but the Kerr coefficient n_2 is maximized at 5 wt.% (25.91×10^{-7} esu) and suppressed at 10 wt.% and 15 wt.% despite a large χ^3, implying loss/dispersion and connectivity effects that diminish effective Kerr refraction. Overall, the central conclusion is that Ag/PANI optical performance is governed by a non-monotonic disorder–dispersion coupling: moderate loading (5 wt.%) provides the most favorable balance of interfacial polarization and manageable loss, producing the best Kerr-type response, whereas higher loading increases carrier-driven dielectric dispersion but can shift the nonlinear response toward dissipative channels and reduce effective n_2. These findings offer a quantitative basis for selecting Ag loading according to target functionality-maximizing Kerr switching at moderate loading versus maximizing carrier-rich dielectric behavior at high loading, and motivate future work that directly links nanoparticle connectivity (e.g., percolation metrics and spatial dispersion state) to a nonlinear figure-of-merit under device-operating wavelengths and intensities.

Author Contributions: Conceptualization, M.A. and T.A.; methodology, M.A. and T.A.; software, M.A. and T.A.; validation, M.A. and T.A.; formal analysis, M.A., T.A., Y.M. and O.M.; investigation, M.A. and T.A.; resources, M.A. and T.A.; data curation, M.A. and T.A.; writing—original draft, M.A. and T.A.; writing—review and editing, M.A. and T.A.; visualization, M.A. and T.A.; supervision, M.A. and T.A.; project administration, M.A. and T.A.; funding acquisition, M.A., T.A., Y.M. and O.M. All authors have read and agreed to the published version of the manuscript.

Funding: This research received no external funding.

Data Availability Statement: The original contributions presented in this study are included in the article. Further inquiries can be directed to the corresponding authors.

Conflicts of Interest: The authors declare no conflicts of interest.

Appendix A. Supporting Information and Data

Appendix A.1. Atomic Force Microscopy (AFM)

Table A1. AFM roughness metrics extracted from the same 20 μm × 20 μm scan areas shown in Figure 2 (tapping mode; 512 × 512 pixels). Areal roughness parameters (S_a, S_q, S_z; with $R_z = z_{max} - z_{min}$). Values are reported in nm; S_z/R_z is additionally reported in nm.

Sample	R_a (nm)	R_q (nm)	R_z (nm)
PANI (pristine)	240.088	303.869	2283.39
Ag/PANI (15 wt.%)	637	830	4740

Appendix A.2. AFM Height-Distribution Histogram of the Pristine PANI Ag/PANI (15 wt.%) Nanocomposite Film

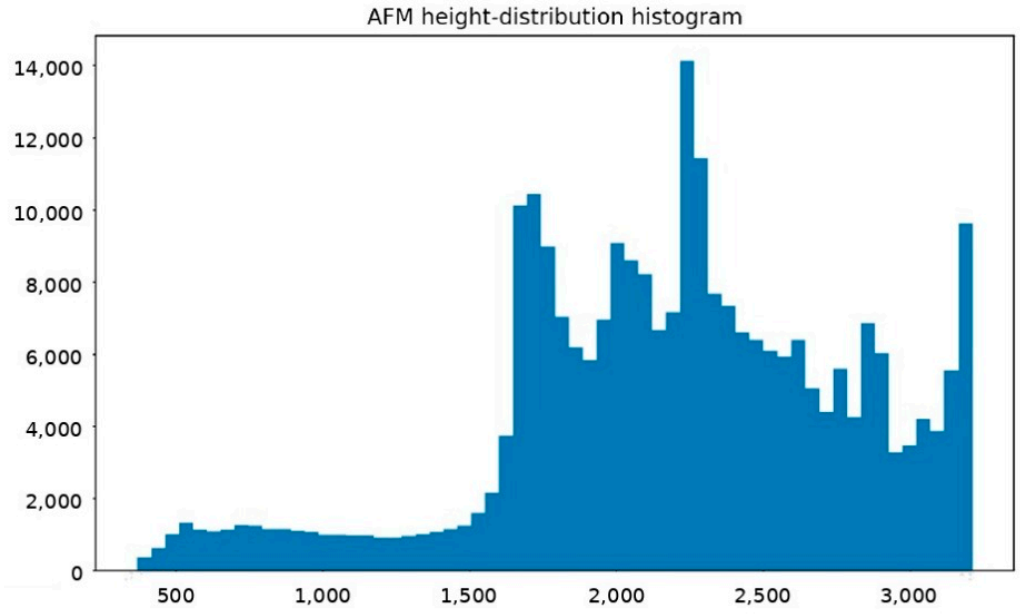


Figure A1. AFM height-distribution histogram of the pristine PANI film recorded over a 20 × 20 μm^2 scan area. The histogram represents the statistical distribution of height values across the scanned surface and provides quantitative insight into the topographic uniformity and roughness of the polymer film.

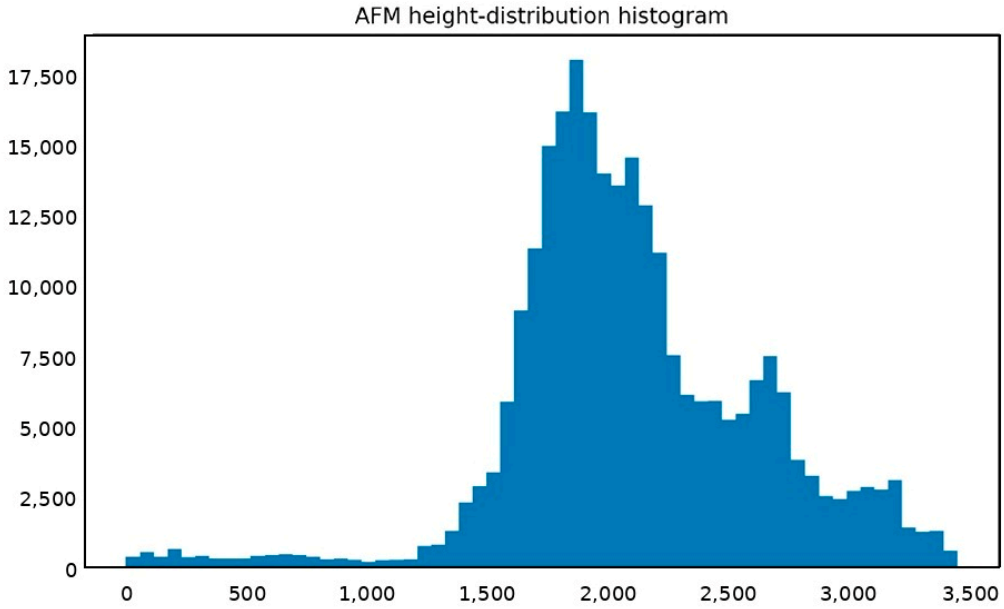


Figure A2. AFM height-distribution histogram of the Ag/PANI (15 wt.%) nanocomposite film recorded over a 20 × 20 μm^2 scan area. The histogram shows the distribution of surface–height values extracted from the AFM topography image, reflecting the surface roughness and height heterogeneity of the film.

Appendix A.3. XRD Analysis

Table A2. FWHM values (from Scherrer crystallite sizes) calculated using the Scherrer relation $D = K\lambda/(\beta \cos\theta)$ rearranged as $\beta = K\lambda/(D \cos\theta)$, where β is the peak full width at half maximum (FWHM) in radians and $\theta = (2\theta)/2$. Assumes K = 0.90 and Cu K_α wavelength λ = 1.5406 Å. FWHM is reported in degrees. If your D values were instrument-corrected, these β values represent the corrected broadening term.

Sample	2θ (deg)	d (Å)	FWHM (deg)	Crystallite Size D (nm)	Phase	hkl
PANI film	9.29	9.513	0.0920	86.6	PANI (emeraldine salt)	
PANI film	15.63	5.665	0.1332	60.2	PANI (emeraldine salt)	
PANI film	18.28	4.848	0.1151	73.3	PANI (emeraldine salt)	(110)
PANI film	22.56	3.938	0.1361	62.3	PANI (emeraldine salt)	(200)
PANI film	27.43	3.250	0.1288	63.5	PANI (emeraldine salt)	
Ag/PANI 5 wt.%	9.44	9.365	0.0900	88.6	PANI (emeraldine salt)	
Ag/PANI 5 wt.%	15.63	5.665	0.1310	61.2	PANI (emeraldine salt)	
Ag/PANI 5 wt.%	18.43	4.810	0.0803	100.2	PANI (emeraldine salt)	(110)
Ag/PANI 5 wt.%	22.56	3.938	0.1537	52.7	PANI (emeraldine salt)	(200)
Ag/PANI 5 wt.%	38.63	2.329	0.0744	113.2	fcc Ag	(111)
Ag/PANI 5 wt.%	44.82	2.020	0.0948	90.6	fcc Ag	(200)
Ag/PANI 10 wt.%	9.29	9.513	0.0936	85.2	PANI (emeraldine salt)	
Ag/PANI 10 wt.%	15.78	5.613	0.1146	70.0	PANI (emeraldine salt)	
Ag/PANI 10 wt.%	18.43	4.810	0.1677	48.0	PANI (emeraldine salt)	(110)
Ag/PANI 10 wt.%	22.56	3.938	0.1750	46.3	PANI (emeraldine salt)	(200)
Ag/PANI 10 wt.%	27.57	3.232	0.1623	50.4	PANI (emeraldine salt)	
Ag/PANI 10 wt.%	38.63	2.329	0.0866	97.2	fcc Ag	(111)
Ag/PANI 10 wt.%	44.82	2.020	0.0846	101.6	fcc Ag	(200)
Ag/PANI 15 wt.%	9.44	9.365	0.0877	90.9	PANI (emeraldine salt)	
Ag/PANI 15 wt.%	15.78	5.613	0.1204	66.6	PANI (emeraldine salt)	
Ag/PANI 15 wt.%	18.58	4.772	0.1078	74.7	PANI (emeraldine salt)	(110)
Ag/PANI 15 wt.%	22.85	3.888	0.1326	61.1	PANI (emeraldine salt)	(200)

Table A2. *Cont.*

Sample	2θ (deg)	d (Å)	FWHM (deg)	Crystallite Size D (nm)	Phase	hkl
Ag/PANI 15 wt.%	27.72	3.216	0.0908	90.1	PANI (emeraldine salt)	
Ag/PANI 15 wt.%	38.78	2.320	0.0762	110.5	fcc Ag	(111)
Ag/PANI 15 wt.%	44.97	2.014	0.0810	106.1	fcc Ag	(200)

References

1. Grosso, D.; Ribot, F.; Boissiere, C.; Sanchez, C. Molecular and supramolecular dynamics of hybrid organic-inorganic interfaces for the rational construction of advanced hybrid nanomaterials. *Chem. Soc. Rev.* **2011**, *40*, 829–848. [CrossRef] [PubMed]
2. Algidsawi, A.J.K.; Hashim, A.; Hadi, A.; Habeeb, M.A. Exploring the characteristics of SnO_2 nanoparticles doped organic blend for low cost nanoelectronics applications. *Semicond. Phys. Quantum Electron. Optoelectron.* **2021**, *24*, 472–477. [CrossRef]
3. Karimi-Maleh, H.; Kumar, B.G.; Rajendran, S.; Qin, J.; Vadivel, S.; Durgalakshmi, D.; Karimi, F. Tuning of metal oxides photocatalytic performance using Ag nanoparticles integration. *J. Mol. Liq.* **2020**, *314*, 113588. [CrossRef]
4. AlZoubi, T.; Kadhem, W.J.; Al Gharram, M.; Makhadmeh, G.; Abdelfattah, M.A.; Abuelsamen, A.; Mourched, B. Advanced Optoelectronic Modeling and Optimization of HTL-Free $FASnI_3$/C60 Perovskite Solar Cell Architecture for Superior Performance. *Nanomaterials* **2024**, *14*, 1062. [CrossRef]
5. AlZoubi, T.; Mourched, B.; Al Gharram, M.; Makhadmeh, G.; Abu Noqta, O. Improving photovoltaic performance of hybrid organic-inorganic $MAGeI_3$ perovskite solar cells via numerical optimization of carrier transport materials (HTLs/ETLs). *Nanomaterials* **2023**, *13*, 2221. [CrossRef] [PubMed]
6. Suriya, P.; Prabhu, M.; Jagannathan, K. Synthesis and structural, optical and photovoltaic characteristics of pure and Ag doped TiO_2 nanoparticles for dye sensitized solar cell application. *Mater. Today Proc.* **2022**, *65*, 100–105. [CrossRef]
7. Al Zoubi, T.; Al-Gharram, M.; Moustafa, M. Insights into the impact of defect states and temperature on the performance of kesterite-based thin-film solar cells. *Optik* **2022**, *264*, 169442. [CrossRef]
8. Oreibi, I.; Ali Habeeb, M.; Abdul Hamza, R.S. Polymer nanocomposites comprising PVA matrix and Ag–$BaTiO_3$ nanofillers: A comparative study of structural, dielectric and optical characteristics for optics and quantum nanoelectronic applications. *Opt. Quantum Electron.* **2024**, *56*, 119. [CrossRef]
9. Parvatikar, N.; Jain, S.; Bhoraskar, S.V.; Ambika Prasad, M.V.N. Spectroscopic and electrical properties of polyaniline/CeO_2 composites and their application as humidity sensor. *J. Appl. Polym. Sci.* **2006**, *102*, 5533–5537. [CrossRef]
10. Al-Gharram, M.; Uhlmann, P.; Al-Hussein, M. Highly dispersed crystalline magnetic and conductive polyaniline/iron oxide nanocomposite films. *Colloids Surf. A Physicochem. Eng. Asp.* **2024**, *684*, 133212. [CrossRef]
11. Frackowiak, E.; Khomenko, V.; Jurewicz, K.; Lota, K.; Béguin, F. Supercapacitors based on conducting polymers/nanotubes composites. *J. Power Sources* **2006**, *153*, 413–418. [CrossRef]
12. Wang, L.; Wu, H.; Chen, L. Polyaniline-Al_2O_3 nanocomposites for electronic applications. *J. Mater. Sci.* **2018**, *53*, 10946–10955. [CrossRef]
13. Dey, A.; De, S.; De, A.; De, S.K. Characterization and dielectric properties of polyaniline–TiO_2 nanocomposites. *Nanotechnology* **2004**, *15*, 1277. [CrossRef]
14. Ahmadi, F. Silver Nanoparticle Enhanced the Optical Properties of the Rare Earth Doped Megnesium Zinc Sulfophosphate Glass. Ph.D. Thesis, University of Technology Malaysia, Johor, Malaysia, 2017.
15. Somani, P.R.; Marimuthu, R.; Mandale, A.B. Synthesis, characterization and charge transport mechanism in conducting polyaniline/V_2O_5 composites. *Polymer* **2001**, *42*, 2991–3001. [CrossRef]
16. Bhadra, S.; Singha, N.K.; Khastgir, D. Polyaniline by new miniemulsion polymerization and the effect of reducing agent on conductivity. *Synth. Met.* **2006**, *156*, 1148–1154. [CrossRef]
17. Majeed Khan, M.A.; Kumar, S.; Ahamed, M.; Alrokayan, S.A.; AlSalhi, M.S. Structural and thermal studies of silver nanoparticles and electrical transport study of their thin films. *Nanoscale Res. Lett.* **2011**, *6*, 434. [CrossRef]
18. Basavaiah, K.; Kumar, Y.P.; Rao, A.V.P. A facile one-pot synthesis of polyaniline/magnetite nanocomposites by micelles-assisted method. *Appl. Nanosci.* **2012**, *3*, 409–415. [CrossRef]
19. AlGharram, M.; AlZoubi, T. Controlled Electrochemical Deposition of Mo/PANI Nanocomposites: Insights into Bandgap Narrowing and DC Charge-Transport in MoO_x/Polyaniline Thin Films. *Ceram. Int.* **2025**, *in press*.
20. Alhazime, A.A.; Benthami, K.; Alsobhi, B.O.; Ali, G.W.; Nouh, S.A. Pani-Ag/PVA nanocomposite: Gamma induced changes in the thermal and optical characteristics. *J. Vinyl Addit. Technol.* **2020**, *27*, 47–53. [CrossRef]
21. Allen, J.P.; Scanlon, D.O.; Watson, G.W. Electronic structures of silver oxides. *Phys. Rev. B* **2011**, *84*, 115141. [CrossRef]
22. Xiao, Q.; Fan, L.H.; Ma, Q.; Ning, Y.M.; Gu, Z.; Chen, L.; Cui, T.J. Secure wireless communication of brain–computer interface and mind control of smart devices enabled by space-time-coding metasurface. *Nat. Commun.* **2025**, *16*, 7914. [CrossRef] [PubMed]

23. Yao, J.; Wang, Z.; Fan, Y.; Zhang, K.; Lin, R.; Wu, J.; Tsai, D.P. Intensity-asymmetric wavefront shaping in nonlocal meta-lens. *Nat. Commun.* **2026**. [CrossRef]
24. Tamboli, M.S.; Kulkarni, M.V.; Patil, R.H.; Gade, W.N.; Navale, S.C.; Kale, B.B. Nanowires of silver–polyaniline nanocomposite synthesized via in situ polymerization and its novel functionality as an antibacterial agent. *Colloids Surf. B Biointerfaces* **2012**, *92*, 35–41. [CrossRef]
25. Al-Gharram, M.; AlZoubi, T. Electrochemical synthesis of a novel hybrid nanocomposite based on Co_3O_4 nanoparticles embedded in PANI-camphor sulfonic acid matrix for optoelectronic applications. *Ceram. Int.* **2024**, *50*, 5473–5482. [CrossRef]
26. Alzoubi, F.; Al-Gharram, M.; AlZoubi, T.; Noqta, O.A.; Makhadmeh, G.; Al-Khateeb, H.; Al-Qadi, M. Advanced electrochemical synthesis and characterization of Al_2O_3 nanoparticles embedded in polyaniline matrix for optoelectronic applications. *Ceram. Int.* **2024**, *50*, 37968–37977. [CrossRef]
27. Al-Gharram, M.; Jum'h, I.; Telfah, A.; Al-Hussein, M. Highly crystalline conductive electrodeposited films of PANI-CSA/$CoFe_2O_4$ nanocomposites. *Colloids Surf. A Physicochem. Eng. Asp.* **2021**, *628*, 127342. [CrossRef]
28. Revenko, A.G.; Tsvetyansky, A.L.; Eritenko, A.N. X-ray fluorescence analysis of solid-state films, layers, and coatings. *Radiat. Phys. Chem.* **2022**, *197*, 110157. [CrossRef]
29. Al-Gharram, M.; AlZoubi, T.; Mandumpal, J. Electrochemical Fabrication and Characterization of CeO_2/PANI Nanocomposite with Enhanced Optoelectronic Performance. *Results Eng.* **2025**, *27*, 106305. [CrossRef]
30. Tauc, J. *Amorphous and Liquid Semiconductors*; Springer: Boston, MA, USA, 1974.
31. Duan, C.; Wang, H.; Ou, X.; Li, F.; Zhang, X. Efficient visible light photocatalyst fabricated by depositing plasmonic Ag nanoparticles on conductive polymer-protected Si nanowire arrays for photoelectrochemical hydrogen generation. *ACS Appl. Mater. Interfaces* **2014**, *6*, 9742–9750. [CrossRef]
32. Kwon, J.; Shin, Y.; Sung, Y.; Doh, H.; Kim, S. Silver sulfide nanocrystals and their photodetector applications. *Accounts Mater. Res.* **2024**, *5*, 1097–1108. [CrossRef]
33. Kanis, D.R.; Ratner, M.A.; Marks, T.J.; Zerner, M.C. Nonlinear optical characteristics of novel inorganic chromophores using the Zindo formalism. *Chem. Mater.* **1991**, *3*, 19–22. [CrossRef]
34. Henaish, A.M.A.; Salem, B.I.; Meaz, T.M.; Alibwaini, Y.A.; Ajlouni, A.W.; Hemeda, O.M.; Arrasheed, E.A. Synthesize, characterization, dielectric, linear and nonlinear optical properties of Ni–Al ferrite/PANI nanocomposite film. *Opt. Mater.* **2021**, *119*, 111397. [CrossRef]
35. Jilani, A.; Othman, M.H.D.; Ansari, M.O.; Khan, I.U.; Hussain, S.Z. Linear/nonlinear optical susceptibility spectroscopic constants of polyaniline@graphene oxide nanocomposite thin films. *Synth. Met.* **2019**, *251*, 30–39. [CrossRef]
36. He, K.; Lu, J.; Ma, X.; Ju, Y.; Xie, L.; Pang, L.; Chen, J. Effect of Maxwell–Wagner relaxation on field charging of particles. *Aerosol Sci. Technol.* **2015**, *49*, 1210–1221. [CrossRef]
37. Palaniappan, S. Chemical and electrochemical polymerization of aniline using tartaric acid. *Eur. Polym. J.* **2001**, *37*, 975–981. [CrossRef]
38. Gupta, K.; Jana, P.C.; Meikap, A.K. Optical and electrical transport properties of polyaniline–silver nanocomposite. *Synth. Met.* **2010**, *160*, 1566–1573. [CrossRef]
39. Verma, A.; Kumar, T. Ag/Cu doped polyaniline hybrid nanocomposite-based novel gas sensor for enhanced ammonia gas sensing performance at room temperature. *RSC Adv.* **2024**, *14*, 25093–25107. [CrossRef]
40. Al-Gharram, M.; AlZoubi, T. Linear and nonlinear optical properties of hybrid Polyaniline/$CoFe_2O_4$ nanocomposites: Electrochemical synthesis, characterization, and analysis. *Ceram. Int.* **2024**, *50*, 32841–32852. [CrossRef]
41. Sakr, G.B.; Yahia, I.S.; Fadel, M.; Fouad, S.S.; Romcevic, N. Optical spectroscopy, optical conductivity, dielectric properties and new methods for determining the gap states of CuSe thin films. *J. Alloys Compd.* **2010**, *507*, 557–562. [CrossRef]
42. Alibwaini, Y.A.; Hemeda, O.M.; El-Shater, R.; Sharshar, T.; Ashour, A.H.; Ajlouni, A.W.; Henaish, A.M.A. Synthesis, characterizations, optical and photoluminescence properties of polymer blend PVA/PEG films doped eosin Y (EY) dye. *Opt. Mater.* **2021**, *111*, 110600. [CrossRef]
43. Benyoucef, M.; Usman, M.A.; Alzoubi, T.; Reithmaier, J.P. Pre-patterned silicon substrates for the growth of III–V nanostructures. *Phys. Status Solidi A* **2012**, *209*, 2402–2410. [CrossRef]
44. Paulraj, P.; Umar, A.; Rajendran, K.; Manikandan, A.; Kumar, R.; Manikandan, E.; Baskoutas, S. Solid-state synthesis of Ag-doped PANI nanocomposites for their end-use as an electrochemical sensor for hydrogen peroxide and dopamine. *Electrochim. Acta* **2020**, *363*, 137158. [CrossRef]
45. Moustafa, M.; Laouini, G.; Alzoubi, T. Finite element analysis of SAW sensor with ZnO substrate for dichloromethane (DCM) gas detection. *Arch. Acoust.* **2021**, *46*, 419–426. [CrossRef]
46. Alzoubi, F.; Al-Gharram, M.; AlZoubi, T.; Al-Khateeb, H.; Al-Qadi, M.; Abu Noqta, O.; Mandumpal, J. Tailoring CuO/Polyaniline Nanocomposites for Optoelectronic Applications: Synthesis, Characterization, and Performance Analysis. *Polymers* **2025**, *17*, 1423. [CrossRef]

47. Tichá, H.; Tichy, L. Semiempirical relation between non-linear susceptibility (refractive index), linear refractive index and optical gap and its application to amorphous chalcogenides. *J. Optoelectron. Adv. Mater.* **2002**, *4*, 381–386.
48. Al-Gharram, M.; AlZoubi, T. Innovative quartz balance technique for vacancies analysis in palladium-hydrogen system. *Ceram. Int.* **2025**, *51*, 31150–31161. [CrossRef]
49. Al-Gharram, M.; Jum'h, I.; Telfah, A.; Al-Hussein, M. PANI-CSA/Co_3O_4 nanocomposite films: Optical, morphological, and structural properties. In *Proceedings of the 2nd International Conference on Industry 4.0 and Artificial Intelligence (ICIAI 2021)*; Atlantis Press: Dordrecht, The Netherlands, 2022; pp. 48–52.
50. AlZoubi, T.; Al-Gharram, M.; Makhadmeh, G.; Noqta, O.A. Comparative analysis of optoelectronic and structural characteristics in electrochemically synthesized hybrid-nanocomposites based on PANI-CSA/metal oxide nanoparticles. *Phys. B Condens. Matter* **2025**, *713*, 417380. [CrossRef]
51. Sathiyanarayanan, S.; Muthukrishnan, S.; Venkatachari, G.; Trivedi, D.C. Corrosion protection of steel by polyaniline (PANI) pigmented paint coating. *Prog. Org. Coat.* **2005**, *53*, 297–301. [CrossRef]
52. Trchová, M.; Stejskal, J. Polyaniline: The infrared spectroscopy of conducting polymer nanotubes (IUPAC Technical Report). *Pure Appl. Chem.* **2011**, *83*, 1803–1817. [CrossRef]
53. Azhakanantham, D.; Al Zoubi, T.; AlGharram, M.; Al-Hmoud, M.; Ibnauof, K.H.; Aldaghri, O.; Kesavan, A.V. Forthright synthesis of titanium-based MXene nanosheets for bio-synaptic device applications: A novel approach. *Ceram. Int.* **2025**, *51*, 259–266. [CrossRef]
54. Nagaraja, M.; Pattar, J.; Shashank, N.; Manjanna, J.; Kamada, Y.; Rajanna, K.; Mahesh, H.M. Electrical, structural and magnetic properties of polyaniline/pTSA-TiO_2 nanocomposites. *Synth. Met.* **2009**, *159*, 718–722. [CrossRef]
55. Mišurović, J.; Mojović, M.; Marjanović, B.; Vulić, P.; Ćirić-Marjanović, G. Magnetite nanoparticles-catalysed synthesis of conductive polyaniline. *Synth. Met.* **2019**, *257*, 116174. [CrossRef]
56. Al-Gharram, M.; AlZoubi, T.; Noqta, O.A.; Makhadmeh, G.N. Comprehensive Study of Linear and Nonlinear Optical Properties of Polyaniline-Al_2O_3 Nanocomposites for Optoelectronic Applications. *Surf. Interfaces* **2024**, *52*, 104939. [CrossRef]
57. Zhang, J.; Zhang, Y.; Li, X.; Yang, B. Nanostructured conducting polymers: Synthesis, morphology, and applications. *Adv. Mater.* **2018**, *30*, 1706574.
58. Al-Gharram, M.; AlZoubi, T. Exploring dual optical responses of polyaniline-Fe_2O_3 nanocomposites for advanced optoelectronic and supercapacitor applications. *Ceram. Int.* **2025**, *in press*. [CrossRef]
59. Lee, Y.H.; Kim, S.H. Enhanced electrochemical performance of conducting polymer nanocomposites through nanoparticle dispersion. *Electrochim. Acta* **2019**, *306*, 606–615.
60. Burdușel, A.C.; Gherasim, O.; Grumezescu, A.M.; Mogoantă, L.; Ficai, A.; Andronescu, E. Biomedical applications of silver nanoparticles: An up-to-date overview. *Nanomaterials* **2018**, *8*, 681. [CrossRef]
61. Ji, X.; Xu, Y.; Zhang, W.; Cui, L.; Liu, J. Review of functionalization, structure and properties of graphene/polymer composite fibers. *Compos. Part A Appl. Sci. Manuf.* **2016**, *87*, 29–45. [CrossRef]
62. Qiu, L.; Zhang, J.; Yang, X. Structural control and enhanced charge transport in nanocomposite materials for energy storage. *J. Mater. Chem. A* **2021**, *9*, 14444–14458.
63. Al-Zoubi, T.; Usman, M.A.; Benyoucef, M.; Reithmaier, J.P. Growth of InAs quantum dots and dashes on silicon substrates: Formation and characterization. *J. Cryst. Growth* **2011**, *323*, 422–425. [CrossRef]
64. Al-Hmoud, M.; Gul, B.; Khan, M.S.; AlGharram, M.; Aziz, S.M.; Al Zoubi, T.; Ahmed, A.M. Insight into novel ErMI (M = S, Se) chalcohalide materials for next-generation energy applications. *RSC Adv.* **2025**, *15*, 34808–34820. [CrossRef]
65. Khairy, M. Synthesis, characterization, magnetic and electrical properties of polyaniline/$NiFe_2O_4$ nanocompo-site. *Synth. Met.* **2014**, *189*, 34–41. [CrossRef]

Disclaimer/Publisher's Note: The statements, opinions and data contained in all publications are solely those of the individual author(s) and contributor(s) and not of MDPI and/or the editor(s). MDPI and/or the editor(s) disclaim responsibility for any injury to people or property resulting from any ideas, methods, instructions or products referred to in the content.